Atmos. Meas. Tech. Discuss., 8, 9399–9453, 2015
www.atmos-meas-tech-discuss.net/8/9399/2015/
doi:10.5194/amtd-8-9399-2015

Atmospheric Measurement Techniques Discussions
Open Access

Interannual variability of upper tropospheric and lower stratospheric (UTLS) region over Ganges–Brahmaputra–Meghna basin based on COSMIC GNSS RO data

Khandu[1], J. Awange[1,2], and E. Forootan[1,3]

[1]Department of Spatial Sciences, Curtin University, Perth, Australia
[2]Geodetic Institute, Karlsruhe University of Technology (KIT), Karlsruhe, Germany
[3]Institute of Geodesy and Geoinformation, University of Bonn, Bonn, Germany

Received: 1 May 2015 – Accepted: 4 August 2015 – Published: 14 September 2015

Correspondence to: Khandu (khandu@postgrad.curtin.edu.au)

Published by Copernicus Publications on behalf of the European Geosciences Union.

Abstract

Poor reliability of radiosonde observational networks across South Asia imposes serious challenges in understanding climate variability and thermodynamic structure of the upper-tropospheric and lower-stratospheric (UTLS) region. The Constellation Observing System for Meteorology, Ionosphere, and Climate (COSMIC) mission launched in April 2006 have overcome many observational limitations that are inherent in conventional atmospheric sounding instruments. This study investigated the interannual variability of the UTLS region over the Ganges–Brahmaputra–Meghna (GBM) basin based on COSMIC radio occultation (RO) data from August 2006 to December 2013. Detailed comparisons were also made with various different radiosonde types and Numerical Weather Prediction (NWP) products. The results indicated that Indian Meteorological Department (IMD) radiosondes performed poorly despite upgrading to newer techniques. ShangE (of China) sonde showed the best agreement with COSMIC RO data with a mean temperature difference of −0.06 °C and a standard deviation of 1.44 °C while the older version (ShangM) indicated a cold bias of 0.61 °C in the UTLS region. The inter-annual variability of temperature in the UTLS region based on COSMIC RO data indicated a clear pattern of El Niño Southern Oscillation (ENSO) and Indian Ocean Dipole (IOD) while the stratospheric temperature anomalies reflected all three major Sudden Stratospheric Warming (SSW) events since 2007. The mean tropopause temperature varied from −70 to −80 °C, with an average height of about 15.5 to 16.3 km from winter to summer, indicating a pronounced annual cycle. The annual amplitudes of tropopause were found to be in the order of 0–6 °C and 0–1.5 km from tropical south to subtropical north. The anomalies of tropopause temperature and height exhibited the patterns of ENSO and IOD exceptionally well with a correlation of 0.65 and −0.52, respectively. The temperature data from Modern-Era Retrospective Analysis for Research Application (MERRA) agreed very well with COSMIC RO data.

AMTD

8, 9399–9453, 2015

Interannual variability of UTLS over the GBM river basin

Khandu et al.

Title Page
Abstract Introduction
Conclusions References
Tables Figures
◂ ▸
Back Close
Full Screen / Esc
Printer-friendly Version
Interactive Discussion

1 Introduction

The interannual variability and change in the vertical structure of the upper-tropospheric/lower-stratospheric (UTLS) region (400–30 hPa) provides key insights into the underlying causes of global and regional aspects of climate change and is closely associated with the surface temperature fluctuations (Karl et al., 2006; Bindoff et al., 2013). The tropopause marks the separation between the two boundary layers in the UTLS region and is a key indicator of global climate change (Santer et al., 2003; Sausen and Santer, 2003) due to its role in tropospheric–stratospheric exchange processes. Observational evidences from balloon-borne radiosondes since the late 1950s and satellite-based measurements since 1979 suggest that the troposphere has warmed considerably over the past decades with substantial cooling in the lower stratosphere (Karl et al., 2006; Bindoff et al., 2013; Lott et al., 2013; Thorne et al., 2013). Much of this temperature changes has been attributed to the anthropogenic emissions of the well-mixed greenhouse gases.

While there is increasing evidence in the recent amplification of global and regional vertical structure of the troposphere and the lower stratosphere (see, e.g., Bindoff et al., 2013), large observational uncertainties exist especially in the UTLS region due to limited observations. As a result, trends in upper air temperatures might be of limited quality, thus, affecting the climate change attribution studies (Seidel et al., 2011; Steiner et al., 2011). Radiosondes can hardly reach up to 50 hPa (∼ 20.5 km) as most of them tend to burst out in the upper tropospheric region. Other issues include instrumental changes over time and poor spatial coverage. Satellite-based Microwave Sounding Units (MSUs) used to retrieve atmospheric information in the UTLS region do not provide adequate vertical resolution and therefore, might indicate systematic biases (Seidel et al., 2011; Bindoff et al., 2013). For example, previous studies reported anomalously large warm biases in radiosonde observations in the South Asian region, particularly over India (see, e.g., Kumar et al., 2010; Sun et al., 2010). In order to improve on these limitations, a more robust space-based technique known as

AMTD

8, 9399–9453, 2015

Interannual variability of UTLS over the GBM river basin

Khandu et al.

the Global Navigation Satellite System (GNSS) radio occultation (RO) (e.g., Melbourne et al., 1994; Ware et al., 1996; Kursinski et al., 1997; Awange, 2012) has emerged as an important climate monitoring system over the past decade (see, e.g., Khandu et al., 2011; Steiner et al., 2013).

GNSS RO technique utilises the time delay information of the occulted GNSS signals, which passes through the atmosphere and is received by Low Earth Orbiting (LEO) satellites. The primary observable are GNSS phase path and signal amplitude, which can be subsequently converted into atmospheric profiles (of e.g., refractivity, temperature) using the assumption of spherical geometry of refractivity (e.g., Melbourne et al., 1994; Rocken et al., 1997). Nowadays, the retrieved bending angles can be directly applied in climate- and weather-related studies, thereby introducing less uncertainty in the observation system (see, e.g., Lewis, 2009). The use of GNSS RO data is advantageous since it provides 24 h global coverage, high vertical resolution, and highly accurate profiles of the upper-tropospheric/lower-stratospheric (UTLS) region (e.g., Sun et al., 2010; Khandu et al., 2011). Therefore, it has continuously been used to analyse the recent variability in the vertical structure in the UTLS region both globally (e.g., Schmidt et al., 2008, 2010) and regionally (e.g., Rao et al., 2009; Fu, 2011; Khandu et al., 2011). The number of RO profiles have increased substantially over the past years with the launch of several GNSS RO missions enabling wider applications in regional studies (see, e.g., Anthes, 2011). For instance, the joint Taiwan-US mission Constellation Observing System for Meteorology, Ionosphere, and Climate (COSMIC)/FORMOSA Satellite Mission 3 (COSMIC/FORMOSAT-3, hereafter, COSMIC) (Anthes et al., 2008) has recorded about 1500 RO soundings per day globally with 70–90 % of the soundings reaching within one km of the Earth's surface.

While many studies have been conducted to re-assess the global as well as regional lower atmospheric structure using the RO profiles, including their accuracies (Rocken et al., 1997; Kuo et al., 2005; Schmidt et al., 2010; Sun et al., 2010; Khandu et al., 2011; Kishore et al., 2011; Danzer et al., 2014), only few such assessments have been carried out over the Indian sub-continent (e.g., Rao et al., 2009). The Ganges–

AMTD
8, 9399–9453, 2015

Brahmaputra–Meghna (GBM) basin in South Asia offers an interesting view on the regional perspective of the variability of UTLS because of its hydrological importance and intense activity of Indian monsoon from June to September. Previous studies have suggested that tropopause heights could be used as an additional indicator of Indian monsoon due to its high correlation with rainfall in May (Kulkarni and Verma, 1993). The rising mountains along the southern foothills of the Himalayas act as barriers to the Indian monsoon generating deep convection along the Himalayan fronts, which may affect the spatial variability of tropopause parameters such as temperature and height. The growing population and expanding industrialisation in and around the GBM river basin are the major source of atmospheric pollution and greenhouse gases (GHGs), and a key modulator of the UTLS region including the tropopause (Gautam et al., 2009; Lau et al., 2009). Thus, long-term self-calibrated GNSS RO data from various LEO missions will help to provide valuable information on the regional climate change in future as indicated by several studies (see, e.g., Schmidt et al., 2008; Steiner et al., 2011, 2013).

This study investigates the interannual variability of temperature in the UTLS region and tropopause parameters (temperatures and heights) over the GBM river basin for the period August 2006 to December 2013 (89 months) using the GNSS RO profiles from the COSMIC RO mission. Further, COSMIC RO data are compared with Modern-Era Retrospective Analysis for Research Application (MERRA, Rienecker et al., 2008) to assess the interannual variability of temperature of the UTLS region. It should be pointed out that no specific study involving MERRA products have been carried over the region. Three specific objectives are outlined as follows; (i) intercompare COSMIC RO retrieved profiles with radiosonde observations and reanalyses products, with specific focus on the upgraded radiosondes over India, (ii) analyse the interannual variability of UTLS temperature (400–30 hPa or 7.5–24.0 km), and (iii) assess the interannual variability of tropopause over the GBM river basin. The use of retrieved parameters such as refractivity, temperature, and water vapour from COSMIC RO data accounts for the overall error budget of the GNSS RO technique.

AMTD
8, 9399–9453, 2015

The remainder of the study is organised as follows. In Sect. 2, the study region is presented. This is followed in Sect. 3 by the description of datasets and methods used, with the interpolation algorithm used to interpolate the point-based COSMIC RO datasets presented in the Appendix. Section 4 discussed the results, and the study concluded in Sect. 5.

2 Ganges–Brahmaputra–Megha (GBM) basin

The GBM river basin in South Asia is a combination of three medium to large river basins, namely, Ganges basin (907 000 km^2), Brahmaputra basin (583 000 km^2) and the Meghna basin (65 000 km^2) (Chowdhury and Ward, 2004). This transboundary river basin with an elevation range from the sea level to more than 8000 m is shared by 5 countries (India (64 %), China (18 %), Nepal (9 %), Bangladesh (7 %) and Bhutan (3 %), see, Fig. 1). The GBM river basin with a total surface area of approximately 1.75 million km^2 features distinct climatic characteristics owing to its diverse climate and other factors such as high topographic variations, the Indian Monsoon, and its interaction with large scale circulations (e.g., Chowdhury, 2003). For instance, Ganges basin is generally characterised by low precipitation while Brahmaputra and Meghna basins are characterised by high rainfall amount (Mirza et al., 1998). The Himalayan fronts (e.g., Meghalayan Plateau) act as an immediate barrier to the summer monsoonal flow and are usually characterized by pronounced rainfall along the Himalayan fronts and across the southern foothills (Barros et al., 2004).

The atmospheric conditions over the basin are largely controlled by the monsoonal circulation during summer (e.g., Kripalani et al., 2007), which is often modulated by global and regional large-scale climate variabilities such as El Niño Southern Oscillation (ENSO) and Indian Ocean Dipole (IOD) (e.g., Chowdhury, 2003; Ashok and Saji, 2007). The impact of global warming and regional climate change arising from increasing population and rapid industrial and agricultural activities, and landuse changes across the basin may have resulted in a warmer troposphere over the years (Gautam et al., 2009; Lau et al., 2009).

3 Data and methods

3.1 FORMOSAT/COSMIC RO data

COSMIC Level 2 RO data analysed at the COSMIC Data Analysis and Archive Center (CDAAC) at the University Corporation for Atmospheric Research (UCAR) for the period August 2006 to December 2013 was used in this study. CDAAC maintains an archive of RO profiles from all previous and existing RO missions such as COSMIC, CHAllenging Minisatellite Payload (CHAMP), Gravity Recovery and Climate Experiment (GRACE), etc. COSMIC is a six-satellite mission launched on the 14 April 2006, with the goal of using GNSS RO data for various atmospheric and weather-related applications (Anthes et al., 2008). With an average sounding of around 1500–2000 profiles per day (at $\sim$ 100 m to 1 km vertical resolution and $\sim$ 300 km horizontal resolution), COSMIC has become a highly successful RO mission with high positive impacts especially on the operational weather forecasts (see e.g., Anthes et al., 2008; Anthes, 2011) and global atmospheric studies (see e.g., Foelsche et al., 2008; Schmidt et al., 2010).

The refractivity (N) and temperature (T) profiles retrieved from raw GNSS signals are referred to as the dry profiles. The raw refractivity profiles are separately processed using a 1-D-Var (one-dimensional variational) analysis with background information from numerical weather forecasts to provide accurate estimates of temperature and humidity in the troposphere. These profiles are referred as the wet profiles and contains information on refractivity, temperature, and water vapour pressure (or relative humidity). CDAAC uses a coarse grid background data from the European Centre for Medium-Range Weather Forecasts (ECMWF) re-analysis (see, http://cdaac-www.cosmic.ucar.edu/cdaac/products.html). The wet and dry profiles mainly differ in the lower troposphere due to presence of water vapour but are highly accurate between 8 and 20 km (see, Anthes et al., 2008). The a priori information (i.e., ECMWF) is minimally influenced by radiosonde observations in the GBM basin as they were not included in ECMWF (Kumar et al., 2010).

The GBM basin received a total of 35 776 profiles from April 2006 to December 2013, at an average of ~ 388 profiles per month (see, Fig. 2a). Figure 2b shows the distribution of COSMIC RO data points at various altitude levels indicating that COSMIC data is able to penetrate deep into the lower troposphere with more than 56 % of the profiles reaching at least 850 hPa (~ 1.5 km above MSL). Figure 3a–d shows the spatial distribution of COSMIC RO data at 850 hPa (~ 1.5 km), 700 hPa (~ 3.1 km), 500 hPa (~ 5.8 km), and 400 hPa (~ 7.5 km), which indicated generally a good correlation with the surface topography of the basin (Fig. 1). The near-complete coverage of the profile data can be seen at 400 hPa (~ 7.5 km) corresponding to the elevation of Himalayas, with Mt. Everest (8848 m) being the highest.

3.2 Radiosonde data

CDAAC also maintains radiosonde records from around the globe, which are collocated with all the RO missions (e.g., COSMIC, CHAMP, GRACE). The radiosonde profiles are extracted from National Center for Atmospheric Research (NCAR) mass store, which is comprehensively described in Sun et al. (2010) including their sources and quality control procedures. There are 24 operational or synoptic radiosonde stations within or around the GBM basin, with most of them operated by the Indian Meteorological Department (IMD) (see, Fig. 1). Three radiosonde stations are located in southern China (or the upper Brahmaputra basin), three are located in southern Bangladesh and the rest (18) of them are located inside the Indian territory. Based on the country of location, these radiosondes differ in their sensor types. The details of the radiosondes are provided in Table 1. The accuracy of IMD radiosondes have been a concern for many years due to their poor performance (see, e.g., Das Gupta et al., 2005; Kumar et al., 2010; Sun et al., 2010) and has undergone major upgrades in the past 5–6 years.

A detailed evaluation of 12 sonde types globally by Sun et al. (2010) from April 2008 to October 2009 showed that IMD radiosondes performed poorly compared to COSMIC RO data while the Shang-E sondes from China suffered from large negative refractivity biases in the mid-troposphere. However, Kumar et al. (2010) reported significant reduction in daily temperature fluctuations at 10 stations, which were prominent before they were upgraded. Therefore, improvements might be expected in humidity measurements. Collocated radiosonde profiles of temperature, water vapour pressure, and refractivity were extracted from CDAAC. Refractivity (N) profiles of radiosonde measurements are derived from observed temperature, T (°C) and water vapour pressure, p_w (hPa) at various pressure, p (hPa) levels based on the relation (Smith and Weintraub, 1953):

$$N = 77.6\frac{p}{T} + 3.73 \times 10^5 \frac{p_\mathrm{w}}{T^2}. \tag{1}$$

There is a comprehensive discussion on the use of various collocation criteria for comparing radiosonde datasets and GNSS RO measurements in e.g., Sun et al. (2010); Anthes (2011), and Khandu et al. (2011). Sun et al. (2010) reported that collocation mismatches impacts the standard deviation errors by up to 0.35–0.42 °C per 3 h and 100 km respectively and ~ 3 % in specific humidity in the lower atmosphere. To maintain an optimum sample size, a collocation criteria of 200 km and 2 h time difference was used in this study to compare the radiosonde measurements and COSMIC profiles.

3.3 MERRA

The Modern-Era Retrospective Analysis for Research Application (MERRA, Rienecker et al., 2008) is a global re-analysis data produced by the state-of-art Goddard Earth Observing System Data Assimilation System, version 5 (GEOS-5) general circulation model (GCM) at National Aeronautic and Space Administration (NASA), US. GEOS-5 assimilates data from a wide variety of observing systems (e.g., in-situ, satellites, etc.),

AMTD
8, 9399–9453, 2015

which are integrated forward in time using a finite-volume dynamics to produce a consistent set of spatio-temporal meteorological and climatic variables since the beginning of the satellite-era (i.e., 1979). An improved land-process model known as the Catchment Land Model has been integrated into the GCM to improve the global hydrological cycle (Rienecker et al., 2008). GEOS-5 is run at a horizontal resolution of $1/2^{\circ} \times 2/3^{\circ}$ (or $\sim 50\,\mathrm{km} \times 70\,\mathrm{km}$) and has 72 vertical layers extending from the surface through to the stratosphere. Atmospheric variables (e.g., temperature, humidity) are produced at various temporal scales ranging from 3 hourly at $1.5^{\circ} \times 1.5^{\circ}$ (or $\sim 150\,\mathrm{km} \times 150\,\mathrm{km}$) spatial resolution), to monthly scales at the nominal horizontal resolution.

GEOS-5 uses radiosondes as the predominant source of information in the model atmosphere, which are further augmented by other atmospheric sensors such as dropsondes, pilot balloons, and raw radiance measurements from satellites (e.g., Advanced MSU) that are weighted according to their observational error variances (see, Rienecker et al., 2008, for details). The variables (e.g., temperature, humidity) are reported at 11 pressure levels for the UTLS region between 400 hPa (~ 7.5 km) to 30 hPa (~ 24.0 km). While radiosondes are sparse in the GBM basin (see, Fig. 1), the MERRA reanalyses products serve as complementary data source in the lower atmosphere in addition to the existing reanalyses products (e.g., ERA-Interim). Here, MERRA temperature in the UTLS region and tropopause parameters (temperatures and heights) were compared with those of COSMIC RO data over the GBM basin for the period August 2006 to December 2013.

3.4 Other datasets

240 collocated profiles, each from two operational forecast products maintained by CDAAC were used as additional data to ascertain the reliability of radiosonde observations over the GBM river basin. The two operational products used are (a) Global Forecast Model (GFS) (Kalnay et al., 1996) from National Centers for Environmental Prediction (NCEP)/NOAA, and (b) ERA-Interim (Dee et al., 2011) from European Centre for Medium-Range Weather Forecasts (ECMWF). Both forecast products have

AMTD
8, 9399–9453, 2015
Interannual variability of UTLS over the GBM river basin
Khandu et al.

been widely used globally to evaluate global as well as regional observations and climate climate models (e.g., Lott et al., 2013; Thorne et al., 2013; Vergados et al., 2015) and are largely independent of the radiosonde datasets over the GBM basin.

3.5 Comparison methods

Accurate and reliable observations of the lower atmosphere are crucial for numerical weather prediction (NWP) and climate change studies. RO data can be used to evaluate the accuracy of different radiosonde types (e.g., Kuo et al., 2005; Sun et al., 2010), as well as helping in identification of error sources in other satellite-based measurements (Ho et al., 2009). In this study, radiosonde observations from within the GBM basin were compared with COSMIC RO profiles for the period August 2006 to December 2013. Mean differences ($\overline{\Delta X}$) and standard deviations (SD_X) of temperature (T) and water vapour pressure (p_w) between radiosondes and RO profiles at various pressure levels were computed as (e.g., Sun et al., 2010):

$$\overline{\Delta X} = \frac{1}{n}\sum_{i=1}^{n}\left(X_i^\mathrm{R} - X_i^\mathrm{C}\right), \tag{2a}$$

$$\mathrm{SD}_X = \sqrt{\frac{1}{n-1}\sum_{i=1}^{n}\left(\left(X_i^\mathrm{R} - X_i^\mathrm{C}\right) - \overline{\Delta X}\right)^2}, \tag{2b}$$

while for refractivity (N), the relative mean differences (Rel. $\overline{\Delta X}$) and standard deviations (Rel. SD_X) were computed as (e.g., Sun et al., 2010):

$$\overline{\Delta X} = \frac{1}{n}\sum_{i=1}^{n}\left(\frac{X_i^\mathrm{R} - X_i^\mathrm{C}}{X_i^\mathrm{C}}\right), \tag{3a}$$

AMTD
8, 9399–9453, 2015

Title Page
Abstract | Introduction
Conclusions | References
Tables | Figures
◀| |▶
◀ ▶
Back | Close
Full Screen / Esc
Printer-friendly Version
Interactive Discussion

$$\mathrm{SD}_X = \sqrt{\frac{1}{n-1}\sum_{i=1}^{n}\left(\frac{\left(X_i^{\mathrm{R}} - X_i^{\mathrm{C}}\right)}{X_i^{\mathrm{C}}} - \overline{\Delta X}\right)^2}, \tag{3b}$$

where X^{R} and X^{C} are the respective radiosonde and COSMIC temperature (T) or water vapour pressure (p_{w}) or refractivity (N), and $i = \{1, 2, \ldots, n\}$ at each pressure level for n data points.

3.6 Interannual variability of the UTLS region

COSMIC RO mission provides an excellent opportunity to assess the interannual variability of the UTLS (subtropical) region with an average of ~ 388 RO profiles per month that are uniformly distributed across the basin since August 2006 (see, Fig. 2). The interannual variability of UTLS temperature was carried out based on the monthly COSMIC RO data and were compared with MERRA products from August 2006 to December 2013. The COSMIC RO data must be gridded for each month over the region to provide a uniform spatial pattern and to provide a fair comparison to MERRA data. The monthly gridded temperature data of COSMIC were averaged for the two regions: (a) UT (400–150 hPa or ~ 7.5–14.2 km) and (b) LS (70–30 hPa or ~ 18.7–24.0 km). The mean temperature data for the two regions were then interpolated to a spatial resolution of 0.5° × 0.5° using the "ordinary kriging" method (details in the Appendix). The geostatistical kriging methods have been shown to be more robust and accurate than other methods such as inverse-distance-weighting, Thiessen Polygons (see, e.g., Goovaerts, 2000; Zhang and Srinivasan, 2009). The UTLS temperature for the MERRA data were obtained by averaging the layers similar to COSMIC data for the same time period. The interannual variability of UTLS temperature was assessed by removing the annual and semi-annual cycles from the time-series of COSMIC and MERRA based on the multilinear regression model. For example, if $\mathbf{X}_{n\times m}$ is a time series of COSMIC or MERRA data with $n = 89$ months and $m = 1404$ grid cells over the GBM river basin, the residual time series ($\hat{\mathbf{X}}_{n\times m}$) can be obtained by:

$$\begin{aligned}\hat{\mathbf{X}} &= \hat{x}(l,j)\\ &= x(l,j) - \left(\hat{\beta}_2(j)\cdot\cos(2\pi t) + \hat{\beta}_3(j)\cdot\sin(2\pi t) + \hat{\beta}_4(j)\cdot\cos(4\pi t) + \hat{\beta}_5(j)\cdot\sin(4\pi t)\right), \end{aligned} \quad (4)$$

where $x(l,j)$ represents an entry of $\mathbf{X}$ from $l = 1,\ldots,n$ and $j = 1,\ldots,m$, and $\hat{\beta}_2$ to $\hat{\beta}_5$ are the regression coefficients representing the linear annual ($\hat{\beta}_2$, $\hat{\beta}_3$) and semi-annual ($\hat{\beta}_4$, $\hat{\beta}_5$) cycles derived by fitting a multilinear regression model using the least squares adjustment technique.

3.7 Tropopause temperatures and heights

The significance of tropopause as a climate indicator has been reported in a number of studies (e.g., Santer et al., 2003; Sausen and Santer, 2003; Khandu et al., 2011; Awange, 2012) and many approaches have been taken to define the tropopause layer based on various atmospheric variables (e.g., temperature, potential vorticity, etc.). This study focusses on the interannual variability of thermal tropopause or "lapse-rate-tropopause" (LRT) derived from COSMIC RO and MERRA data over the GBM river basin. According to WMO (1957), LRT is the lowest level at which lapse rate decreases to less than 2 °C km^{-1} and the average lapse rate between the lowest level and anywhere above that level up to 2 km remains less than 2 °C km^{-1}. The tropopause heights and temperatures from COSMIC data have already been computed by CDAAC, while MERRA provides tropopause temperature based on the WMO (1957) definition. The tropopause height, h_{LRT} (in km) for MERRA reanalysis was approximated from the tropopause pressure, p (in hPa) using the following relationship (PSAS, 2004):

$$h_{\mathrm{LRT}} \equiv 44\,330.8 - 4946.54 \times p^{0.1902632}. \quad (5)$$

Discussion Paper | Discussion Paper | Discussion Paper | Discussion Paper |

AMTD

8, 9399–9453, 2015

Interannual variability of UTLS over the GBM river basin

Khandu et al.

4 Results and discussion

4.1 Comparison of radiosonde and COSMIC RO data

The quality of radiosonde types with respect to GNSS RO data has been reported in a number of studies (e.g., Rocken et al., 1997; Hajj et al., 2004; Ho et al., 2009; Sun et al., 2010; Steiner et al., 2011; Wang et al., 2013) and their overall agreement with COSMIC RO data has been found to be less than 0.15 °C with a standard deviation of 1.5–2.0 °C (e.g., Sun et al., 2010). In this section, the quality of different radiosondes across the GBM river basin (see, Table 1) were assessed using COSMIC RO profiles between August 2006 and December 2013. Of particular interest is the performance of the recently upgraded radiosondes at three stations in India: New-Delhi, Patna, and Dirbugarh. Statistical comparisons were made with respect to temperature, water vapour pressure, and refractivity using a collocation criteria of 200 km and 2 h between COSMIC RO data and radiosonde observations. While a more closer collocation criteria was deemed necessary for comparison due to drifts in radiosondes and tangent point horizontal drifts in GNSS RO data (Sun et al., 2010; Wang et al., 2013), the more relaxed criteria was used here considering the low number of samples at some stations such as those over Bangladesh and China. The number of collocated data points varied at each pressure level for both temperature and humidity (i.e., water vapour pressure) as most radiosondes tend to malfunction or burst out before reaching the lower stratosphere as shown in Fig. 4.

4.1.1 Temperature

Figure 5 shows the mean temperature difference and their standard deviations at 12 pressure levels from 850–30 hPa (or 1.5–24 km) of various radiosonde types against COSMIC RO data over the GBM basin. Their mean difference and standard deviations in the UTLS region are presented in Table 2. The quality of radiosondes differ highly among different sonde types with the closest agreement shown by ShangE indicating

AMTD
8, 9399–9453, 2015

a mean difference of −0.06 °C and a standard deviation of 1.44 °C in the UTLS region (see, Table 2). The ShangM sonde showed a slightly larger (cold) bias between 400 and 100 hPa (7.5–16.6 km) with an average standard deviation of around 2 °C (Fig. 5). Radiosonde observations (of two types) from 3 stations over Bangladesh indicated a large positive (warm) bias (> 0.5 °C) above 250 hPa (or 10.9 km) with standard deviations of more than 3 °C (Fig. 5). Their overall accuracy in the UTLS region was around 0.62–0.88 °C with a standard deviation of 3.19–3.57 °C (see, Table 2). Note that the number of RO data points vary along the vertical profile as radiosondes tend to burst out before reaching the lower stratosphere (Table 2). Their overall differences showed relatively warmer biases in the lower atmosphere (below 200 hPa). However, they were usually cancelled out by cold bias in the upper regions (see Table 2).

On the other hand, the IMD-MK4 radiosondes showed anomalously large bias and standard deviations indicating both cold bias (up to 2.3°) in the upper troposphere (400–150 hPa; 7.5–14.2 km) and warm bias (up to 5 °C) above 150 hPa (or 14.2 km) (see, Fig. 5a). Their standard deviations ranges from 2–7 °C from 850 to 30 hPa (see, Fig. 5b), which were consistent with the previous studies (e.g., Kumar et al., 2010; Sun et al., 2010). In order to see if there were any improvement at the three radiosonde stations (New Delhi, Patna, and Dilbugarh), a separate analysis was carried out using observations before (August 2006–May 2009) and after (June 2009–May 2013), i.e., the upgrading period. The analysis showed dismal improvement in temperature measurements (see, Fig. 5) but showed a relatively smaller bias in the UTLS region with a mean difference of 1.2 °C and a standard deviation of 4.1 °C (see, Table 2). Kumar et al. (2010) reported that large diurnal temperature fluctuations found in previous observations were reduced significantly at the 10 upgraded stations across India.

4.1.2 Water vapour

Water vapour plays an important role in the global and regional weather, climate, and hydrology but also is a major source of uncertainty in the lower atmosphere contributing to about 3–4 % of the error in refractivity at near surface in moist regions (e.g., Kuo et al., 2004; Danzer et al., 2014). Water vapour pressure retrieved at CDAAC is based on the 1-D-Var assimilation system that uses a priori information from ECMWF, which also contains radiosonde observations and hence not fully independent. Nevertheless, the IMD radiosonde observations were mostly not included in the ECMWF model (Kumar et al., 2010), and could therefore highlight important differences against the COSMIC RO data. Figure 6 shows the mean difference and standard deviations of water vapour pressures from the radiosonde observations with respect to those from COSMIC RO data. All the radiosonde observations showed dry bias (of up to 30 %) above 500 hPa (or 5.8 km) with respect to COSMIC RO data, with ShangE and ShangM indicating relatively larger biases than the rest of the sonde types (Fig. 6a). However, radiosonde observations over Bangladesh and India (MK4) showed considerably wetter biases below 500 hPa. The standard deviation errors (Fig. 6b) ranges from 0 in the upper troposphere (where water vapour is negligent) to more than 100 % (or up to 3 hPa) at the near-surface at 850 hPa (1.5 km).

4.1.3 Refractivity

Errors in refractivity are directly related to errors in observed temperatures and water vapour with the later contributing the most in the lower troposphere. The comparison results shown in Fig. 7 indicated very large relative errors in IMD sondes (∼ 5 %) corresponding to their very warm biases in the tropopause region (see, Fig. 5a), while radiosonde observations over Bangladesh tend to show mean errors of less than 1 % because of their relatively smaller biases. ShangE sonde showed the best performance above 300 hPa (or 9.6 km) indicating a relative bias of less than 0.25 % while its counterpart ShangM sonde was also better than those from India and Bangladesh. The results of ShangE/ShangM sondes were consistent with the findings of Sun et al. (2010), which reported generally negative (0.3 %) fractional errors in the lower troposphere and positive (0.1 %) errors in the stratosphere (see, also, Table 2). The relative standard deviations of refractivity derived from various radiosonde types shown in Fig. 7b largely resembles the standard deviation of the temperature difference (Fig. 5b) ranging

AMTD
8, 9399–9453, 2015

from about 5 % (IMD) to less than 1 % (ShangE/ShangM). Thus, very large refractivity errors in IMD sondes in the upper troposphere may have resulted from anomalously warm bias (see, Fig. 5a) and possible errors in pressure measurements.

4.2 Comparison of COSMIC RO data and Numerical Weather Prediction (NWP) model outputs

To assess how radiosondes observations differ from the NWP outputs over the GBM river basin, especially in the lower GBM river basin where IMD sondes performed poorly, a brief analysis was carried out by comparing NWP outputs from ERA-Interim and GFS models, radiosonde observations, and COSMIC profiles for the year 2012. The year 2012 was adopted arbitrarily in order to confirm the statistical results of radiosondes in the region, and thus, radiosonde observations were also included in the analysis. Mean differences and standard deviations of temperature, water vapour pressure, and refractivity were computed for the year 2012 based on the COSMIC RO data using the collocation criteria of 200 km radius and a time difference of 2 h from a radiosonde observation. Only 175 profiles were found to match this criteria, with all of them located over India and Bangladesh. First, to assess how each product differed over the individual stations, Fig. 8 plots the skew-T / log-P over four stations from west to east of the GBM river basin: (a) Patialia (#42101), (b) Siliguri (#42397), (c) Dilbugarh (#42314), and (d) Chittagong (#41977). The skew-T / log-P chart is a commonly used thermodynamic diagram to help forecasters determine the relative humidity, stability, vertical wind shear, severe weather, and flash flood potential of the atmosphere. In a Skew-T / log-P chart, the y axis is the pressure (in hPa) in a log scale (black dashed lines), temperature is skewed at 45° (solid black lines), moist adiabatic (in red lines), mixing ratio (in green lines), and dry adiabatic (in blue lines).

The NWP products generally showed good agreement with the COSMIC RO data above 400 hPa (or ~ 7.32 km) but showed slightly larger difference below 400 hPa. The dry profiles of COSMIC RO data on the other hand, tend to deviate away from wet profile at around 300–400 hPa. The radiosonde observations showed very good agree-

AMTD
8, 9399–9453, 2015

ment at Patialia (Fig. 8a) and Chittagong (Fig. 8d) but showed warm bias at Dilrugarh (Fig. 8c). The overall accuracy of the NWP data in the UTLS for temperature and refractivity and in the lower troposphere for water vapour pressure are provided in Table 3. The results indicate that both ERA-Interim and GFS data showed good agreement with COSMIC RO data, which far exceeded the quality of radiosonde data over the GBM river basin. For example, the mean temperature differences of ERA-Interim and GFS data were 0.15 °C with a standard deviation of around 1.0 °C while radiosonde data showed a mean difference and a standard deviation of 1.22 and 3.94 °C, respectively.

4.3 Interannual variability of the UTLS region

Figure 9 shows the seasonal variability of temperature in the UTLS region over the GBM river basin from August 2006 to December 2013. The temperature in the UT region was marked by a strong seasonal pattern indicating a difference of up to 10 °C between the lower and the upper peaks (Fig. 9a and b). The strong seasonality gradually diminishes and became nearly constant in the tropopause layer between 150 and 70 hPa (14–18.5 km) indicating a much wider tropopause belt in the region. This supports the view that tropopause is no more a thin layer (see, Fueglistaler et al., 2009). The temperature pattern in the stratosphere (above 18.5 km) was relatively stable without much seasonality but exhibited sudden fall in temperature during the early months of 2008, 2009, and 2013. These cooling events have been reported to be associated with Sudden Stratospheric Warming (SSW) events in the winter polar regions (Hansen et al., 2014). The stratosphere responds to major global climatic events (e.g., Brewer–Dobson circulation), solar radiations, and natural and man-made aerosol forcings (e.g., Fueglistaler et al., 2009), and have been found to influence global weather conditions in the lower troposphere (e.g., Foelsche et al., 2008; Seidel et al., 2011). The SSW events in the winter polar region have been found to be associated with significant cooling (of about 1 °C) of the stratosphere over low latitude and equatorial regions (Fritz and Soules, 1972).

AMTD
8, 9399–9453, 2015

The MERRA data (Fig. 9b) was found to agree very well above 12.5 km indicating a difference of only ±1 °C (Fig. 9c) but indicated large differences in the tropospheric region with a difference of up to ±3 °C. The amplitudes of COSMIC RO data were found to be lower in the lower troposphere with a slightly delayed temperature maximum in the region. The lower amplitudes in COSMIC RO (Fig. 9a) could have resulted from the low resolution background information used to retrieve RO temperature in the troposphere (Kuo et al., 2004).

To further understand the dynamics of the UTLS region over the GBM basin, the interannual variability of temperature of the UTLS region was assessed. The temporal temperature patterns were derived by removing the annual and semi-annual cycles from the basin-averaged time series of COSMIC RO and MERRA data (see, Eq. 4). The de-seasonalised time series were compared with large-scale ocean-atmospheric phenomena such as ENSO and IOD, which were found to significantly influence the seasonal climate fluctuations in the GBM river basin (see, e.g., Chowdhury and Ward, 2004; Ashok and Saji, 2007). ENSO is commonly represented by sea surface temperature (SST) anomalies such as those within the Niño3.4 region (5° N–5° S, 120–170° W) (Trenberth, 1990), while IOD is commonly measured by the difference between SST anomalies in the western (50–70° E and 10° S–10° N) and eastern (90–110° E and 10–0° S) equatorial Indian Ocean, which is referred to as Dipole Mode Index (Saji et al., 1999). Monthly ENSO index (Niño3.4) from the Climate Prediction Center (CPC, http://www.cpc.ncep.noaa.gov/products/analysis_monitoring/ensostuff/) and DMI (as IOD index) from the Low-latitude Climate Prediction Research (http://www.jamstec.go.jp/frcgc/research/d1/iod/iod/dipole_mode_index.html) were used.

In addition, comparisons were also made with Quasi-Biennial Oscillation(QBO) index at 30 hPa, which were extracted from the NOAA website (http://www.esrl.noaa.gov/psd/data/climateindices/list/). QBO or formally known as Singapore Winds is a quasiperiodic oscillation of the equatorial zonal wind between the easterlies and westerlies in the tropical stratosphere where the downward propagating winds are finally dissipated at the tropical tropopause region, with a mean period of about 28 months (Baldwin

AMTD
8, 9399–9453, 2015

et al., 2001). The variability of QBO in the lower stratospheric temperature can induce interannual variability in the tropopause temperature (Baldwin et al., 2001). QBO is measured by an index derived from the zonally averaged easterlies at 50–30 hPa above the equatorial region.

Figure 10a and b shows the interannual variability of temperature in the UT and LS, respectively, together with the corresponding temporal patterns of QBO, ENSO (Niño3.4), and IOD (DMI) over the period from August 2006 to December 2013. The temporal patterns of temperature in UT and LS region were found to exhibit the patterns of all three climate indices with varying degree of magnitudes. The ENSO activity heightened during the past 5 years with two major warm phases (i.e., El Niño or +ive Niño3.4) in 2006/07 and 2009/10 and four major cold phases (i.e., La Niña or -ive Niño3.4) during the periods 2007/08, 2008/09, 2010/11, and 2011/12 (see, Fig. 10). These cold (warm) ENSO phases are associated with extreme drought conditions (flooding) in the GBM river basin with further contribution from IOD activities, which may also act independently during the neutral ENSO periods (e.g., Chowdhury, 2003; Ashok and Saji, 2007).

The stratospheric temperature showed a maximum amplitude of −3 °C during the winter of 2008/09 (Fig. 10a) corresponding to the major SSW event (e.g., Resmi et al., 2013; Hansen et al., 2014) whereas the maximum amplitude (3 °C) of tropospheric temperature was found to occur in the winter of 2011/12 corresponding to a moderate La Niña period (Fig. 10b). Similarly, the stratospheric cooling in the winter of 2012/13 were associated with a major SSW event (see, http://gmao.gsfc.nasa.gov/researchhighlights/SSW/) but has negligible impact on the tropospheric variability. The stratospheric temperature increases (decreases) during the positive El Niño (La Niña) periods (Fig. 10a) while the tropospheric temperature showed the opposite, indicating an increase in temperature during the warm ENSO phase (Fig. 10b). Thus, both stratospheric and tropospheric temperature shows very good correlation with ENSO pattern with a magnitude of 0.44 (for stratospheric temperatures) and −0.62 (for tropospheric temperatures) based on the COSMIC RO data even for a very short period of time (see, Table 4). The MERRA data showed a slightly better correlation with ENSO but indicated a lag of approximately one month with respect to the tropospheric temperature. This lag can be found especially during the periods of 2008/09, 2010/11, and 2013 but generally agrees very well with COSMIC RO data.

The relationship between IOD and UTLS was found to follow the ENSO pattern indicating positive correlation during the warm ENSO phases and negative correlation during the cold phases of ENSO (see, Fig. 10). The correlation between IOD and tropospheric temperature based on the 89 months of COSMIC RO data was −0.59 with a lag of 7 months (see, Table 4). Similar results were shown by MERRA data for the same lag period. Since QBO is a stratospheric phenomenon, it has greater influence on the stratospheric temperature than on the tropospheric temperature. As a result, QBO has been found to be highly correlated with the stratospheric temperature (0.5 to −0.5).

4.4 Tropopause heights and temperatures over GBM basin

The seasonal and interannual variations of tropopause temperatures and heights over the GBM river basin were investigated. Figure 11 shows the frequency distribution of tropopause temperatures and heights based on the COSMIC RO data only. The tropopause exhibited a clear seasonal variation over the GBM basin with lower and warmer tropopause during winter (DJF, i.e., Fig. 11a and e), and higher and colder tropopause during the summer (JJA, i.e., Fig. 11c) and autumn (SON, i.e., Fig. 11d). The tropopause height varied between 10 km and a little over 18.5 km corresponding to a temperature of −40 °C and around −85 °C. Large variations were seen especially during the spring (MAM) with a standard deviation of 9.6 °C and 2.2 km, respectively (Fig. 11b and f). This strong variation of tropopause in spring could be due to high diurnal (day and night) variations, which tend to be in the order of ∼ 1 km and ∼ 3 °C over the region (Mehta et al., 2010).

To further illustrate the seasonal variations of the tropopause, Figs. 12 and 13 shows the spatial distribution of annual and semi-annual amplitudes of tropopause temper-

AMTD
8, 9399–9453, 2015

atures and heights (i.e., mean annual variation) derived from MERRA and COSMIC RO data. These annual and semi-annual amplitudes were derived from the multilinear regression model described in Eq. (4). The highest amplitudes were found over the subtropics (north of 26°) where the tropopause temperatures wwere found to vary by almost 8 °C (Fig. 12a and c) and tropopause heights varied by up to 2 km in the same region (Fig. 13a and c). The semi-annual variations of tropopause temperatures (Fig. 12b and d) and heights (Fig. 13b and d) were relatively small (with a maximum of 0.4 °C and 0.15 km, respectively). It is interesting to note that the magnitude of variations in tropopause temperatures increased sharply along 26° N (Fig. 12a and c) while the tropopause heights' variations were found to be more steeper along northern boundary of the GBM river basin. The spatial patterns of amplitudes derived from MERRA data as shown in Figs. 12c and 13c were found to be consistent with COSMIC RO data, but MERRA indicated larger temperature variations while its height variations were less than 1.5 km.

To be more precise on the seasonal variation of tropopause over the region, the mean annual cycle of tropopause temperatures and heights with their standard deviations are plotted in Fig. 14. The seasonal variation of tropopause indicated a strong annual cycle following the Indian monsoon over the GBM river basin. The minimum tropopause temperature of COSMIC RO data was found to occur during the peak monsoon period (July) while the maximum temperature was found to occur in January (Fig. 14a). On the other hand, the tropopause height peaks in June and reaches its minimum in January (Fig. 14b). The tropopause variations (represented by error bars) were found to be very small during the monsoon period (June–September) and substantially high from November to May. Such variations could be related to synaptic scale (day-to-day) variability of the regional atmospheric convection over the region (Mehta et al., 2010). The day-to-day variations can be particulary large when the small-scale convective activities dominate the regional atmosphere between November and May. Both the dataset indicated strong annual cycle but tropopause was found to be warmer (by 2–5 °C) and lower (by 1 km) over the GBM basin. Earlier studies have

AMTD
8, 9399–9453, 2015
Interannual variability of UTLS over the GBM river basin
Khandu et al.

also reported warm biases in reanalysis products compared to GNSS RO data and radiosonde observations (e.g., Randel et al., 2000).

While it is impossible to derive long-term trends and variability of the tropopause using COSMIC RO data, a short-term (89 months) interannual variability of the tropopause temperatures and heights has been carried out here. Since tropopause is a transitional layer between the troposphere and the stratosphere, both tropospheric activities such as ENSO and IOD and stratospheric activities such as QBO and SSW events can have significant influence on the temporal variations of tropopause heights and temperatures (Randel et al., 2000). The de-seasonalised temporal anomalies (using Eq. 4) (i.e., deviation from mean) of tropopause temperatures and heights of COSMIC RO data have been compared with those from MERRA data to assess the temporal variability of tropopause over the region.

Figure 15 shows the interannual variability of tropopause temperatures and heights derived from COSMIC RO and MERRA data for the period between August 2006 and December 2013, as well as the indices of QBO, ENSO (Niño3.4), and IOD (DMI). The tropopause temperature of COSMIC RO data exhibited the patterns of ENSO (Niño3.4) and IOD (-DMI) very well (Fig. 15a) with a correlation of 0.65 and −0.38, respectively, which were equally represented by the MERRA data (Table 5). While ENSO lags tropopause temperature by one month, IOD was found to appear earlier by 6 months as indicated by both the dataset. For instance, the tropopause warmed by about 2 °C during the major El Niño event of 2009/10 and a cooling of similar magnitude has occurred during the major La Niña period of 2010/11 (see, Fig. 15a).

While the tropopause cools as a result of major SSW events in the northern polar region, even though with a lesser magnitude in this study, the major SSW event of 2009 was found to have a large impact on the tropopause heights (Fig. 15b). The tropopause height increased by more than 2 km over the region as indicated by the MERRA data. However, COSMIC RO data showed an increase of only about 1 km. ENSO and IOD events were still found to dominate the temporal variation of tropopause heights in the region, which showed a correlation of −0.52 and 0.33 (based on COSMIC RO data)

AMTD
8, 9399–9453, 2015

and lag (lead) of one (six) months, respectively. MERRA data indicated a slightly higher correlation with ENSO and IOD. The increase in tropopause temperature during the El Niño conditions were associated with an equivalent decrease in tropopause heights (e.g., 2009/10). Furthermore, the tropopause heights showed a similar decrease during the early months of 2013 after a moderate El Niño event (with contributions from IOD).

The QBO is a well-known stratospheric phenomenon, which has been reported to have greater influence on the tropical tropopause characteristics (e.g., Reid and Gage, 1985; Randel et al., 2000). The relationship between tropopause and QBO signal over the GBM river basin (in the sub-tropical region) was found to be quite complex mainly because of the ∼ 28 month cycle of the QBO signal (Baldwin et al., 2001), which cannot be properly captured in the temporal period defined in this study. The peak-to-peak time differences of maximum correlation (0.4 to −0.5) between tropopause (temperatures and heights) and QBO signals was around 30 months, consistent with the cycle of QBO signal (figures not shown).

5 Conclusions

Several GNSS RO missions were launched in the past decade to provide high-quality, global observations of the Earth's atmosphere (ionosphere, stratosphere, and troposphere) for various weather and climate applications. This study examined the interannual variability of temperature in the upper troposphere/lower stratosphere (UTLS) region as well as the tropopause over the GBM river basin in South Asia using 89 months (August 2006 to December 2013) of COSMIC RO data. The GBM basin received a total of 35 776 COSMIC RO profiles over the study period, with an average of ∼ 388 well-distributed profiles/month from August 2006–December 2013. More than 56 % of the profiles reached at least 1.5 km above the mean sea level height. Radiosonde observations from 24 stations in and around the GBM river basin were compared with COSMIC RO data to assess the quality of on-going monitoring work in the region. ShangE/China radiosondes showed the best agreement with a mean temperature dif-

Discussion Paper | Discussion Paper | Discussion Paper | Discussion Paper |

AMTD

8, 9399–9453, 2015

Interannual variability of UTLS over the GBM river basin

Khandu et al.

ference of −0.06 °C and standard deviation of 1.44 °C followed by ShangM/China and those over Bangladesh. The IMD radiosondes still exhibited large warm biases and anomalously high variations in the UTLS region even after upgrading their radiosondes at three stations. However, from the data period used in this study, the mean temperature differences were observed to have reduced by more than half (2.72 to 1.20 °C) after upgrading.

The temporal anomalies of UTLS (400–30 hPa; 7.5–24.0 km) temperatures exhibited clear temporal patterns of ENOS/IOD modes while also adequately capturing the major sudden stratospheric warming (SSW) events of 2009 and 2013. Overall, the tropospheric temperature anomalies indicated very good correspondence with ENSO (Niño3.4 index) and IOD (DMI index) with negative correlations of 0.62 and 0.59, respectively. The MERRA data performed equally well with even higher correlation in this study. Based on COSMIC RO data, the mean tropopause temperature was found to vary between −70 to −80 °C with an average height of about 15.5 to 16.3 km from winter to summer over the GBM river basin, thus, exhibiting a strong annual cycle in the region. The annual amplitudes of tropopause temperatures varied considerably from the tropics to the sub-tropics (0 to 5 °C) while the corresponding tropopause heights varied from 0 to 1.5 km.

Both tropopause temperature and height anomalies over the GBM river basin exhibited strong temporal patterns of ENSO indicating a correlation of 0.65 and −0.52, respectively, with a lag of one month, and were equally represented by the MERRA data. The IOD also indicated reasonably good correspondence with tropopause temperatures and heights with a correlation of −0.38 and 0.33, and with a lag of six and five months, respectively. While QBO has a well-known interannual signal, which significantly impacts the variability of tropopause in the tropics, its correlation with tropopause over the GBM river basin varied between 0.4 to −0.5 with a peak-to-peak time difference of ∼ 30 months. The tropopause heights were found to be sensitive to the recent SSW events of 2008/09, but were not properly captured during the last two SSW events

AMTD
8, 9399–9453, 2015

of 2009/10 and 2012/13 due probably to strong combined influences of ENSO and IOD events.

Appendix

The ordinary kriging method uses a semi-variogram to characterize the spatial variability of the variable (Z) at a point of analysis grid (x_0). The unknown value $Z(x_0)$ is interpreted as a random variable located in x_0 and is the linear combination of observed values ($z_i = Z(x_i)$) and weights $\gamma_i(x_0)$ from neighbouring locations ($i = 1,\ldots,N$) obtained by (e.g., Goovaerts, 2000):

$$\hat{Z}(x_0) = \sum_{i=1}^{N} \gamma_i(x_0) \times Z(x_i), \quad \text{where} \sum_{i=1}^{N} \gamma_i(x_0) = 1. \tag{A1}$$

An experimental semi-variogram $\hat{\gamma}(h)$ is calculated for each month as (e.g., Goovaerts, 2000):

$$\hat{\gamma}(h) = \frac{1}{2N(h)} \sum_{i}^{N(h)} [Z(x_i) - Z(x_i + h)]^2, \tag{A2}$$

where h is the distance between two points, $N(h)$ is the number of pairs separated by distance h, $Z(x_i)$ are the observed values at x_i, and $Z(x_i + h)$ are the observed values at the next point separated by h. A theoretical semi-variogram (e.g., gaussian, spherical, exponential, etc.,) is modelled to Eq. (A2) to minimise the error variance and to optimise smoothing. Figure 16 shows an example of three theoretical semi-variograms fitted to the experimental semi-variogram of COSMIC-derived tropopause temperature for September 2008. The tropopause temperature is rather spatially homogeneous over the GBM basin for September 2008 indicating a relatively homogenous surface until about 15° (or ~ 1500 km). This indicates the scale of the atmospheric variability as

Discussion Paper | Discussion Paper | Discussion Paper | Discussion Paper |

AMTD
8, 9399–9453, 2015

opposed to a complex terrain and its associate weather in the region. Based on our experiments we have adopted the spherical model for all the months.

Acknowledgements. The first author deeply appreciates Curtin Strategic International Research Scholarship, Curtin University (Australia) for funding his PhD studies. He is further grateful to Intergovernmental Panel of Climate Change (IPCC) for the scholarship. J. L. Awange is grateful to the Alexander von Humboldt foundation for supporting his stay at the Geodetic Institute, Karlsruhe Institute of Technology (KIT). E. Forootan is grateful for the research grant from the German Aerospace Center (DLR, D-SAT project-Fkz: 50 LZ 1402) and the research grant provided by WASM/TIGeR, Curtin University (Australia). The authors are highly grateful to the COSMIC Data Analysis and Archival Center (CDAAC, http://cdaac-www.cosmic.ucar.edu/cdaac/) for providing both COSMIC radio occultation profiles, regional radiosonde datasets, and re-analysis profiles used in this study. The authors are also thankful to the MERRA for providing high-resolution global atmospheric products for regional studies. This is a TiGeR publication number (635).

References

Anthes, R. A.: Exploring Earth's atmosphere with radio occultation: contributions to weather, climate and space weather, Atmos. Meas. Tech., 4, 1077–1103, doi:10.5194/amt-4-1077-2011, 2011. 9402, 9405, 9407

Anthes, R. A., Ector, D., Hunt, D. C., Kuo, Y. H., Rocken, C., Schreiner, W. S., Sokolovskiy, S. V., Syndergaard, S., Wee, T. K., Zeng, Z., Bernhardt, P. A., Dymond, K. F., Chen, Y., Liu, H., Manning, K., Randel, W. J., Trenberth, K. E., Cucurull, L., Healy, S. B., Ho, S. P., McCormick, C., Meehan, T. K., Thompson, D. C., and Yen, N. L.: The COSMIC/FORMOSAT-3 mission: early results, B. Am. Meteorol. Soc., 89, 313–333, doi:10.1175/BAMS-89-3-313, 2008. 9402, 9405, 9406

Ashok, K. and Saji, N. H.: On the impacts of ENSO and Indian Ocean dipole events on sub-regional Indian summer monsoon rainfall, Nat. Hazards, 42, 273–285, doi:10.1007/s11069-006-9091-0, 2007. 9404, 9417, 9418

Awange, J. L.: GNSS remote sensing of the environment, in: Environmental Monitoring Using GNSS: Global Navigation Satellite Systems, Springer, Berlin Heidelberg, p. 382, 2012. 9402, 9411

Baldwin, M. P., Gray, L. J., Dunkerton, T. J., Hamilton, K., Haynes, P. H., Randel, W. J., Holton, J. R., Alexander, M. J., Hirota, I., Horinouchi, T., Jones, D. B. A., Kinnersley, J. S., Marquardt, C., Sato, K., and Takahashi, M.: The quasi-biennial oscillation, Rev. Geophys., 39, 179–229, doi:10.1029/1999RG000073, 2001. 9417, 9418, 9422

Barros, A. P., Kim, G., Williams, E., and Nesbitt, S. W.: Probing orographic controls in the Himalayas during the monsoon using satellite imagery, Nat. Hazards Earth Syst. Sci., 4, 29–51, doi:10.5194/nhess-4-29-2004, 2004. 9404

Bindoff, N. L., Stott, P. A., AchutaRao, K. M., Allen, M. R., Gillett, N., Gutzler, D., Hansingo, K., Hegerl, G., Hu, Y., Jain, S., Mokhov, I. I., Overland, J., Perlwitz, J., Sebbari, R., and Zhang, X.: Detection and attribution of climate change, in: Climate Change 2013: The Physical Science Basis. Contribution of Working Group I to the Fifth Assessment Report of the Intergovernmental Panel on Climate Change, edited by: Stocker, T. F., Qin, D., Plattner, G.-K., Tignor, M., Allen, S., Boschung, J., Nauels, A., Xia, Y., Bex, V., and Midgley, P., Cambridge University Press, Cambridge, UK and New York, NY, USA, 867–952, 2013. 9401

Chowdhury, M. R.: The El Niño-Southern Oscillation (ENSO) and seasonal flooding – Bangladesh, Theor. Appl. Climatol., 76, 105–124, doi:10.1007/s00704-003-0001-z, 2003. 9404, 9418

Chowdhury, M. D. R. and Ward, N.: Hydro-meteorological variability in the greater Ganges–Brahmaputra–Meghna basins, Int. J. Climatol., 24, 1495–1508, doi:10.1002/joc.1076, 2004. 9404, 9417

Danzer, J., Foelsche, U., Scherllin-Pirscher, B., and Schwärz, M.: Influence of changes in humidity on dry temperature in GPS RO climatologies, Atmos. Meas. Tech., 7, 2883–2896, doi:10.5194/amt-7-2883-2014, 2014. 9402, 9414

Das Gupta, M., Das, S., Prasanthi, K., and Pradhan, P. K.: Validation of upper-air observations taken during the ARMEX-I and its impact on the global analysis-forecast system, Mausam, 56, 139–146, 2005. 9406

Dee, D. P., Uppala, S. M., Simmons, A. J., Berrisford, P., Poli, P., Kobayashi, S., Andrae, U., Balmaseda, M. A., Balsamo, G., Bauer, P., Bechtold, P., Beljaars, A. C. M., van de Berg, L., Bidlot, J., Bormann, N., Delsol, C., Dragani, R., Fuentes, M., Geer, A. J., Haimbergere, L., Healy, S. B., Hersbach, H., Holm, E. V., Isaksen, L., Kållberg, P., Köhler, M., Matricardi, M., McNally, A. P., Monge-Sanz, B. M., Morcrette, J.-J., Park, B.-K., Peubey, C., de Rosnay, P., Tavolato, C., Thépaut, J.-N., and Vitarta, F.: The ERA-Interim reanalysis: configuration

AMTD
8, 9399–9453, 2015

and performance of the data assimilation system, Q. J. Roy. Meteor. Soc., 137, 553–597, doi:10.1002/qj.828, 2011. 9408

Foelsche, U., Borsche, M., Steiner, A. K., Gobiet, A., Pirscher, B., Kirchengast, G., Wickert, J., and Schmidt, T.: Observing upper troposphere–lower stratosphere climate with radio occultation data from the CHAMP satellite, Clim. Dynam., 31, 49–65, doi:10.1007/s00382-007-0337-7, 2008. 9405, 9416

Fritz, S. and Soules, S. D.: Planetary variations of stratospheric temperatures, Mon. Weather Rev., 100, 582–589, 1972. 9416

Fu, E.: An Investigation of GNSS Radio Occultation Atmospheric Sounding Technique for Australian Meteorology, PhD thesis, School of Mathematical and Geospatial Sciences, College of Science, Engineering and Health, RMIT University, Melbourne, Victoria, Australia, 2011. 9402

Fueglistaler, S., Dessler, A. E., Dunkerton, T. J., Folkins, I., Fu, Q., and Mote, P. W.: Tropical tropopause layer, Rev. Geophys, 47, RG1004, doi:10.1029/2008RG000267, 2009. 9416

Gautam, R., Hsu, N. C., Lau, K. M., Tsay, S. C., and Kafatos, M.: Enhanced pre-monsoon warming over the Himalayan-Gangetic Region from 1979 to 2007, Geophys. Res. Lett., 36, L07704, doi:10.1029/2009GL037641, 2009. 9403, 9405

Goovaerts, P.: Geostatistical approaches for incorporating elevation into the spatial interpolation of rainfall, J. Hydrol., 228, 113–129, doi:10.1016/S0022-1694(00)00144-X, 2000. 9410, 9424

Hajj, G. A., Ao, C. O., Iijima, B. A., Kuang, D., Kursinski, E. R., Mannucci, A. J., Meehan, T. K., Romans, L. J., de la Torre Juarez, M., and Yunck, T. P.: CHAMP and SAC-C atmospheric occultation results and intercomparisons, J. Geophys. Res., 109, D06109, doi:10.1029/2003JD003909, 2004. 9412

Hansen, F., Matthes, K., Petrick, C., and Wang, W.: The influence of natural and anthropogenic factors on major stratospheric sudden warmings, J. Geophys. Res., 119, 8117–8136, doi:10.1002/2013JD021397, 2014. 9416, 9418

Ho, S. P., Goldberg, M., Kuo, Y. H., Zou, C. Z., and Schreiner, W.: Calibration of temperature in the lower stratosphere from microwave measurements using COSMIC radio occultation data: preliminary results, Terr. Atmos. Ocean. Sci., 20, 87–100, doi:10.3319/TAO.2007.12.06.01(F3C), 2009. 9409, 9412

Kalnay, E., Kanamitsu, M., Kistler, R., Collins, W., Deaven, D., Gandin, L., Iredell, M., Saha, S., White, G., Woollen, J., Zhu, Y., Chelliah, M., Ebisuzaki, W., Higgins, W., Janowiak, J., Mo, K. C., Ropelewski, C., Wang, J., Leetmaa, A., Reynolds, R., Jenne, R., and Joseph, D.:

AMTD
8, 9399–9453, 2015

The NCEP/NCAR 40-year reanalysis project, B. Am. Meteorol. Soc., 77, 437–470, 1996. 9408

Karl, T. R., Hassol, S. J., Miller, C. D., and Murray, W. L. (Eds.): Temperature Trends in the Lower Atmosphere: Steps for Understanding and Reconciling Differences, Tech. rep., U.S. Climate Change Science Program, Washington, DC, 2006. 9401

Khandu, Awange, J. L., Wickert, J., Schmidt, T., Sharifi, M. A., Heck, B., and Fleming, K.: GNSS remote sensing of the Australian tropopause, Climate Change, 105, 597–618, doi:10.1007/s10584-010-9894-6, 2011. 9402, 9407, 9411

Kishore, P., Ratnam, M. V., Namboothiri, S., Velicogna, I., Basha, G., Jiang, J., Igarashi, K., Rao, S., and Sivakumar, V.: Global (50° S–50° N) distribution of water vapor observed by COSMIC GPS RO: comparison with GPS radiosonde, NCEP, ERA-Interim, and JRA-25 reanalysis data sets, J. Atmos. Sol.-Terr. Phy., 17, 1849–1860, doi:10.1016/j.jastp.2011.04.017, 2011. 9402

Kripalani, R. H., Oh, J. H., Kulkarni, A., Sabade, S. S., and Chaudhari, H. S.: South Asian summer monsoon precipitation variability: coupled climate model simulations and projections under IPCC AR4, Theor. Appl. Climatol., 90, 133–159, doi:10.1007/s00704-006-0282-0, 2007. 9404

Kulkarni, J. R. and Verma, R. K.: On the spatio-temporal variations of the tropopause height over India and Indian summer monsoon activity, Adv. Atmos. Sci., 10, 481–488, doi:10.1007/BF02656973, 1993. 9403

Kumar, G., Madan, R., Krishnan, K. S., and Jain, P. K.: Upgradation of Indian Radiosonde Network: Performance and Future Plans, Tech. rep., India Meteorological Department, Lodi Road, New Delhi, India, 2010. 9401, 9406, 9407, 9413, 9414

Kuo, Y. H., Wee, T. K., Sokolovskiy, S., Rocken, C., Schreiner, W., Hunt, D., and Anthes, R. A.: Inversion and error estimation of GPS radio occultation data, J. Meteorol. Soc. Jpn., 82, 507–531, doi:10.1029/2004GL021443, 2004. 9414, 9417

Kuo, Y.-H., Schreiner, W. S., Wang, J., Rossiter, D. L., and Zhang, Y.: Comparison of GPS radio occultation soundings with radiosondes, Geophys. Res. Lett., 32, L05817, doi:10.1029/2004GL021443, 2005. 9402, 9409

Kursinski, E. R., Hajj, G. A., Schofield, J. T., Linfield, R. P., and Hardy, K. R.: Observing Earth's atmosphere with radio occultation measurements using the Global Positioning System, J. Geophys. Res., 102, 23429–23465, doi:10.1029/97JD01569, 1997. 9402

Lau, W. K. M., Kim, K. M., Hsu, C. N., and Holben, B. N.: Possible influences of air pollution, dust- and sandstorms on the Indian monsoon, Bulletin – World Meteorological Organization, 58, 22–30, 2009. 9403, 9405
Lewis, H. W.: A robust method for tropopause altitude identification using GPS radio occultation data, Geophys. Res. Lett., 36, L12808, doi:10.1029/2009GL039231, 2009. 9402
Lott, F. C., Stott, P. A., Mitchell, D. M., Christidis, N., Gillett, N. P., Haimberger, L., Perlwitz, J., and Thorne, P. W.: Models versus radiosondes in the free atmosphere: a new detection and attribution analysis of temperature, J. Geophys. Res., 118, 2609–2619, doi:10.1002/jgrd.50255, 2013. 9401, 9409
Mehta, S. K., Ratnam, M. V., and Murthy, B. V. K.: Variability of the tropical tropopause over Indian monsoon region, J. Geophys. Res., 115, D14120, doi:10.1029/2009JD012655, 2010. 9419, 9420
Melbourne, W. G., Davis, E. S., Duncan, C. B., Hajj, G. A., Hardy, K. R., Kursinski, E. R., Meehan, T. K., Young, L. E., and Yunck, T. P.: The application of spaceborne GPS to atmospheric limb sounding and global change monitoring, Tech. Rep. JPL-PUBL-94-18, Jet Propulsion Laboratory, California Institute of Technology, Pasadena, CA, US, 1994. 9402
Mirza, M. M. Q., Warrick, R., Ericksen, N., and Kenny, G.: Trends and persistence in precipitation in the Ganges, Brahmaputra and Meghna river basins, Hydrological Sciences, 43, 845–858, doi:10.1080/02626669809492182, 1998. 9404
PSAS: A quick derivation relating altitude to air pressure, Portland State Aerospace Society, US, available at: http://psas.pdx.edu/RocketScience/PressureAltitude_Derived.pdf, 2004. 9411
Randel, W. J., Wu, F., and Gaffen, D. J.: Interannual variability of the tropical tropopause derived from radiosonde data and NCEP reanalyses, J. Geophys. Res., 105, 15509–15523, doi:10.1029/2000JD900155, 2000. 9421, 9422
Rao, D. N., Ratnam, M. V., Mehta, S., Nath, D., Basha, S. G., Rao, V. V. M. J., Murthy, B. V. K., Tsuda, T., and Nakamura, K.: Validation of the COSMIC radio occultation data over Gadanki (13.48° N, 79.2° E): a tropical region, Terr. Atmos. Ocean. Sci., 20, 59–70, doi:10.3319/TAO.2008.01.23.01(F3C), 2009. 9402
Reid, G. C. and Gage, K. S.: Interannual variations in the height of the tropical tropopause, J. Geophys. Res., 90, 5629–5635, doi:10.1029/JD090iD03p05629, 1985. 9422
Resmi, E., Mohanakumar, K., and Appu, K.: Effect of polar sudden stratospheric warming on the tropical stratosphere and troposphere and its surface signatures over the Indian region, B. Am. Meteorol. Soc., 105–106, 15–29, doi:10.1016/j.jastp.2013.07.003, 2013. 9418

Rienecker, M. M., Suarez, M. J., Todling, R., Bacmeister, J., Takacs, L., Liu, H. C., Gu, W., Sienkiewicz, M., Koster, R. D., Gelaro, R., Stajner, I., and Nielsen, J. E.: The GEOS-5 Data Assimilation System Documentation of Versions 5.0.1, 5.1.0, and 5.2.0, NASA Technical Report Series on Global Modeling and Data Assimilation Vol. 27, NASA/TM–2008–104606, NASA Center for AeroSpace Information, Greenbelt, Maryland, US, 2008. 9403, 9407, 9408

Rocken, C., Anthes, R., Exner, M., Hunt, D., Sokolovskiy, S., Ware, R., Gorbunov, M., Schreiner, W., Feng, D., Herman, B., Kuo, Y.-H., and Zou, X.: Analysis and validation of GPS/MET data in the neutral atmosphere, J. Geophys. Res., 102, 29849–29866, doi:10.1029/97JD02400, 1997. 9402, 9412

Saji, N. H., Goswami, B. N., Vinayachandran, P. N., and Yamagata, T.: A dipole mode in the tropical Indian Ocean, Nature, 401, 360–363, 1999. 9417

Santer, B. D., Wehner, M. F., Wigley, T. M. L., R., Meehl, G. A., Taylor, K. E., Ammann, C., Arblaster, J., Washington, W. M., Boyle, J. S., and Brüggemann, W.: Contributions of anthropogenic and natural forcing to recent tropopause height changes, Science, 301, 479–483, doi:10.1126/science.1084123, 2003. 9401, 9411

Sausen, R. and Santer, B. D.: Use of changes in tropopause height to detect human influences on climate, Meteorol. Z., 3, 131–136, doi:10.1127/0941-2948/2003/0012-0131, 2003. 9401, 9411

Schmidt, T., Wickert, J., Beyerle, G., and Heise, S.: Global tropopause height trends estimated from GPS radio occultation data, Geophys. Res. Lett., 35, L11806, doi:10.1029/2008GL034012, 2008. 9402, 9403

Schmidt, T., Wickert, J., and Haser, A.: Variability of the upper troposphere and lower stratosphere observed with GPS radio occultation bending angles and temperatures, Adv. Space Res., 46, 150–161, doi:10.1016/j.asr.2010.01.021, 2010. 9402, 9405

Seidel, D. J., Gillett, N. P., Lanzante, J. R., Shine, K. P., and Thorne, P. W.: Stratospheric temperature trends: our evolving understanding, WIREs Climate Change, 2, 592–616, doi:10.1002/wcc.125, 2011. 9401, 9416

Smith, E. K. and Weintraub, S.: The constants in the equation for atmospheric refractive index at radio frequencies, Proceedings of the IRE, 41, 1035–1037, doi:10.1109/JRPROC.1953.274297, 1953. 9407

Steiner, A. K., Lackner, B. C., Ladstädter, F., Scherllin-Pirscher, B., Foelsche, U., and Kirchengast, G.: GPS radio occultation for climate monitoring and change detection, Radio Sci., 46, RS0D24, doi:10.1029/2010RS004614, 2011. 9401, 9403, 9412

AMTD
8, 9399–9453, 2015

Interannual variability of UTLS over the GBM river basin

Khandu et al.

Steiner, A. K., Hunt, D., Ho, S.-P., Kirchengast, G., Mannucci, A. J., Scherllin-Pirscher, B., Gleisner, H., von Engeln, A., Schmidt, T., Ao, C., Leroy, S. S., Kursinski, E. R., Foelsche, U., Gorbunov, M., Heise, S., Kuo, Y.-H., Lauritsen, K. B., Marquardt, C., Rocken, C., Schreiner, W., Sokolovskiy, S., Syndergaard, S., and Wickert, J.: Quantification of structural uncertainty in climate data records from GPS radio occultation, Atmos. Chem. Phys., 13, 1469–1484, doi:10.5194/acp-13-1469-2013, 2013. 9402, 9403

Sun, B., Reale, A. J. D., and Hunt, D. C.: Comparing radiosonde and COSMIC atmospheric profile data to quantify differences among radiosonde types and the effects of imperfect collocation on comparison statistics, J. Geophys. Res., 115, D23104, doi:10.1029/2010JD014457, 2010. 9401, 9402, 9406, 9407, 9409, 9412, 9413, 9414

Thorne, P. W., Brohan, P., Titchner, H. A., McCarthy, M. P., Sherwood, S. C., Peterson, T. C., Haimberger, L., Parker, D. E., Tett, S. F. B., Santer, B. D., Fereday, D. R., and Kennedy, J. J.: A quantification of uncertainties in historical tropical tropospheric temperature trends from radiosondes, J. Geophys. Res., 116, D12116, doi:10.1029/2010JD015487, 2013. 9401, 9409

Trenberth, K. E.: Recent observed interdecadal climate changes in the Northern Hemisphere, B. Am. Meteorol. Soc., 71, 988–993, doi:10.1175/1520-0477(1990)071<0988:ROICCI>2.0.CO;2, 1990. 9417

Vergados, P., Mannucci, A. J., Ao, C. O., Jiang, J. H., and Su, H.: On the comparisons of tropical relative humidity in the lower and middle troposphere among COSMIC radio occultations and MERRA and ECMWF data sets, Atmos. Meas. Tech., 8, 1789–1797, doi:10.5194/amt-8-1789-2015, 2015. 9409

Wang, B.-R., Liu, X.-Y., and Wang, J.-K.: Assessment of COSMIC radio occultation retrieval product using global radiosonde data, Atmos. Meas. Tech., 6, 1073–1083, doi:10.5194/amt-6-1073-2013, 2013. 9412

Ware, R., Rocken, C., Solheim, F., Exner, M., Schreiner, W., Anthes, R., Feng, D., Herman, B., Gorbunov, M., Sokolovskiy, S., Hardy, K., Kuo, Y., Zou, X., Trenberth, K., Meehan, T., Melbourne, W., and Businger, S.: GPS sounding of the atmosphere from low earth orbit: preliminary results, B. Am. Meteorol. Soc., 77, 19–40, doi:10.1175/1520-0477(1996)077<0019:GSOTAF>2.0.CO;2, 1996. 9402

WMO: Meteorology – a three-dimensional science: second session of the commission for aerology, WMO Bulletin, IV, 134–138, 1957. 9411

AMTD
8, 9399–9453, 2015

Interannual variability of UTLS over the GBM river basin

Khandu et al.

Zhang, X. and Srinivasan, R.: GIS-based spatial precipitation estimation: a comparison of geostatistical approaches, J. Am. Water Resour. As., 45, 894–906, doi:10.1111/j.1752-1688.2009.00335.x, 2009. 9410

Table 1. Details of various types of radiosondes used in and around the GBM river basin between August 2006 to December 2013. The upgraded IMD radiosondes were named as GPS (Global Positioning Sytem) sondes.

SL/No	WMO ID	Make	Location/Country	Latitude	Longitude	MSL [m]	# Profiles
1	42 101	IMD MK4	PATIALA/INDIA	30°20′ N	76°28′ E	251	1354
2	42 182	GPS Sonde	NEW DELHI/INDIA	28°35′ N	77°12′ E	216	2937
3	42 314	GPS Sonde	DIBRUGARH/INDIA	27°29′ N	95°1′ E	111	1687
4	42 339	IMD MK4	JODHPUR/INDIA	26°18′ N	73°1′ E	224	1142
5	42 361	IMD MK4	GWALIOR/INDIA	26°14′ N	78°15′ E	207	245
6	42 369	IMD MK4	LUCKNOW/INDIA	26°45′ N	80°53′ E	128	1244
7	42 379	IMD MK4	GORAKHPUR/INDIA	26°45′ N	83°22′ E	77	864
8	42 397	IMD MK4	SILIGURI/INDIA	26°40′ N	88°22′ E	123	432
9	42 410	IMD MK4	GAUHATI/INDIA	26°6′ N	91°35′ E	54	810
10	42 492	GPS Sonde	PATNA/INDIA	25°36′ N	85°6′ E	60	1066
11	42 647	IMD MK4	AHMADABAD/INDIA	23°4′ N	72°38′ E	55	1366
12	42 667	IMD MK4	BHOPAL/INDIA	23°17′ N	77°21′ E	523	1011
13	42 701	IMD MK4	RANCHI/INDIA	23°19′ N	85°19′ E	652	1248
14	42 724	IMD MK4	AGARTALA/INDIA	23°53′ N	91°15′ E	16	681
15	42 809	IMD MK4	CALCUTTA/INDIA	22°39′ N	88°27′ E	6	2537
16	42 867	IMD MK4	NAGPUR /INDIA	21°6′ N	79°3′ E	310	908
17	42 874	IMD MK4	RAIPUR/INDIA	21°14′ N	81°39′ E	298	655
18	42 971	IMD MK4	BHUBANESWAR/INDIA	20°15′ N	85°50′ E	46	1662
19	41 923	VRS92G	DHAKA/BDESH	23°46′ N	90°23′ E	9	843
20	41 977	Unknown	CHITTAGONG/BDESH	22°21′ N	91°49′ E	34	210
21	41 883	Unknown	BOGRA/BDESH	24°51′ N	89°22′ E	20	21
22	56 137	Shang/M	QAMDO/CHINA	31°9′ N	97°10′ E	3307	908
23	55 591	Shang/E	LHASA/CHINA	29°40′ N	91°8′ E	3650	264
24	55 299	Shang/E	NAGQU/CHINA	31°29′ N	92°4′ E	4508	2664

AMTD
8, 9399–9453, 2015

Table 2. Comparison of COSMIC RO data and observed soundings of different radiosondes used in and around the GBM river basin between August 2006 and December 2013. The number of collocated profiles slightly vary between temperatures and refractivities. The statistics were computed for the UTLS region (400–30 hPa) for temperatures and refractivities, and in the lower troposphere (850–200 hPa) for the water vapour pressures.

Radiosonde Types	ΔT (°C)	$\sigma\Delta T$ (°C)	Δp_w (hPa)	$\sigma\Delta p_w$ (hPa)	ΔN (%)	$\sigma\Delta N$ (%)	# Profiles (T/N)
unknown [Bdesh]	0.62	3.57	0.037	0.673	−0.32	1.37	161/161
Vaisala RS92 [Bdesh]	0.88	3.19	0.004	0.597	−0.42	1.11	134/134
MK4 [IMD]	2.77	4.97	0.058	0.090	−1.47	2.29	2292/2271
ShangE [China]	−0.06	1.44	−0.174	0.254	−0.26	0.88	657/657
ShangM [China]	−0.61	1.98	−0.186	0.193	0.02	1.05	247/247
Comparison between MK4 and GPS sondes at 3 stations in India							
MK4 [IMD]	2.72	4.01	−0.020	1.073	−1.39	1.88	271/270
GPS-sonde [IMD]	1.20	4.09	−0.142	0.686	−0.68	1.84	314/310

AMTD
8, 9399–9453, 2015
Interannual variability of UTLS over the GBM river basin
Khandu et al.

Table 3. Comparison of COSMIC RO data and observed soundings of different radiosondes used in and around the GBM river basin between August 2006 to December 2013. The number of collocated profiles slightly vary between temperature and refractivity. The temperature and refractivity statistics were computed for the UTLS region (400–30 hPa) and in the lower troposphere (850–200 hPa), the water vapour pressure statistics were computed.

Data	ΔT (°C)	$\sigma\Delta T$ (°C)	Δp_w (hPa)	$\sigma\Delta p_w$ (hPa)	ΔN (%)	$\sigma\Delta N$ (%)
Radiosonde	1.22	3.94	0.11	0.95	−0.64	1.83
ERA	0.15	0.99	0.07	0.41	−0.06	0.49
GFS	0.15	1.04	−0.01	0.47	−0.07	0.51

AMTD
8, 9399–9453, 2015

Table 4. Correlation coefficients between UTLS temperature and climate indices between August 2006 to December 2013.

Climate Index	Stratospheric Temperature		Tropospheric Temperature	
	COSMIC	MERRA	COSMIC	MERRA
Nino3.4	0.44 (0)	0.54 (1)	−0.62 (1)	−0.67 (1)
DMI	0.26 (0)	0.39 (1)	−0.59 (−7)	−0.56 (−7)

AMTD
8, 9399–9453, 2015

Table 5. Correlation coefficients (and time lags in months) between tropopause parameters (temperature and height) and climate indices between August 2006 to December 2013.

Climate Index	Tropopause Temperature		Tropopause Height	
	COSMIC	MERRA	COSMIC	MERRA
Nino3.4	0.65 (1)	0.71 (1)	−0.52 (1)	−0.62 (1)
DMI	−0.38 (−6)	−0.38 (−6)	0.33 (−5)	0.37 (−5)

AMTD
8, 9399–9453, 2015

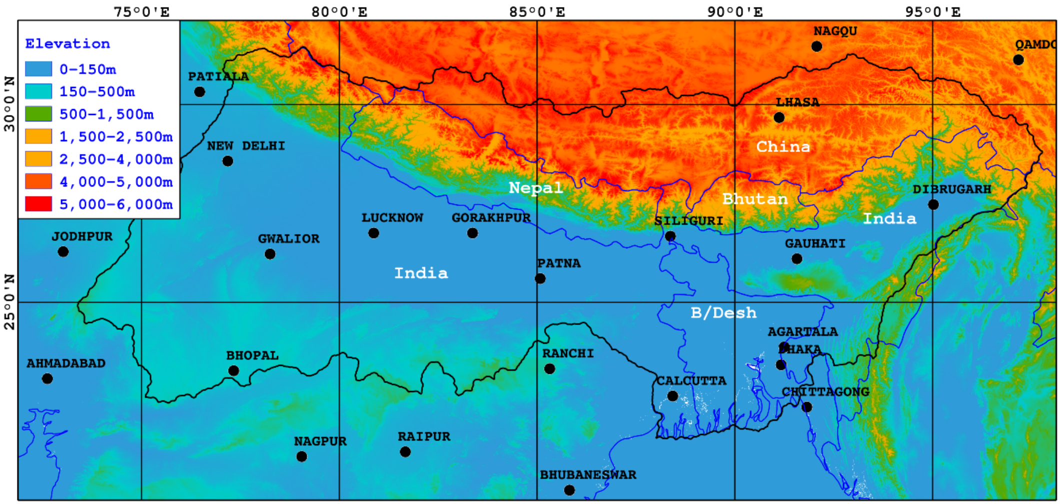

Figure 1. Elevation of the Ganges–Brahmaputra–Meghna basin in South Asia. The digital elevation model is derived from the Shuttle Radar Topography mission (SRTM, http://srtm.csi.cgiar.org). The locations of the existing radiosonde stations are are shown in circles (black).

AMTD
8, 9399–9453, 2015

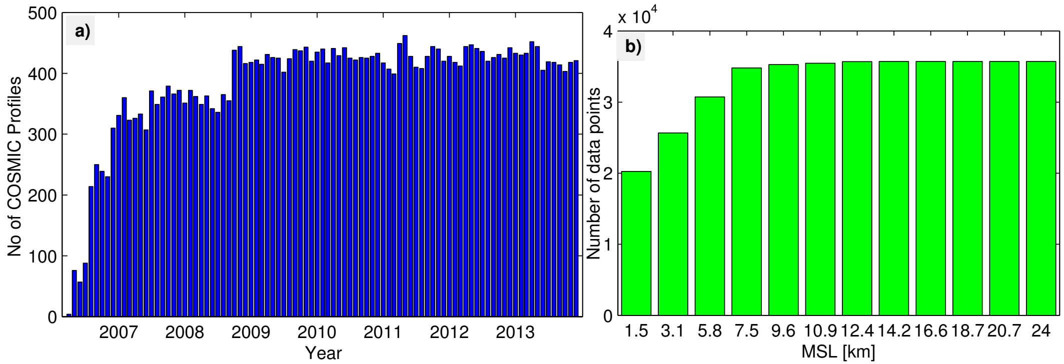

Figure 2. (a) Number of COSMIC RO profiles reported in and around the GBM basin between April 2006 and December 2013, and **(b)** the corresponding number of data points at each pressure levels 850–30 hPa (1.5–24.0 km).

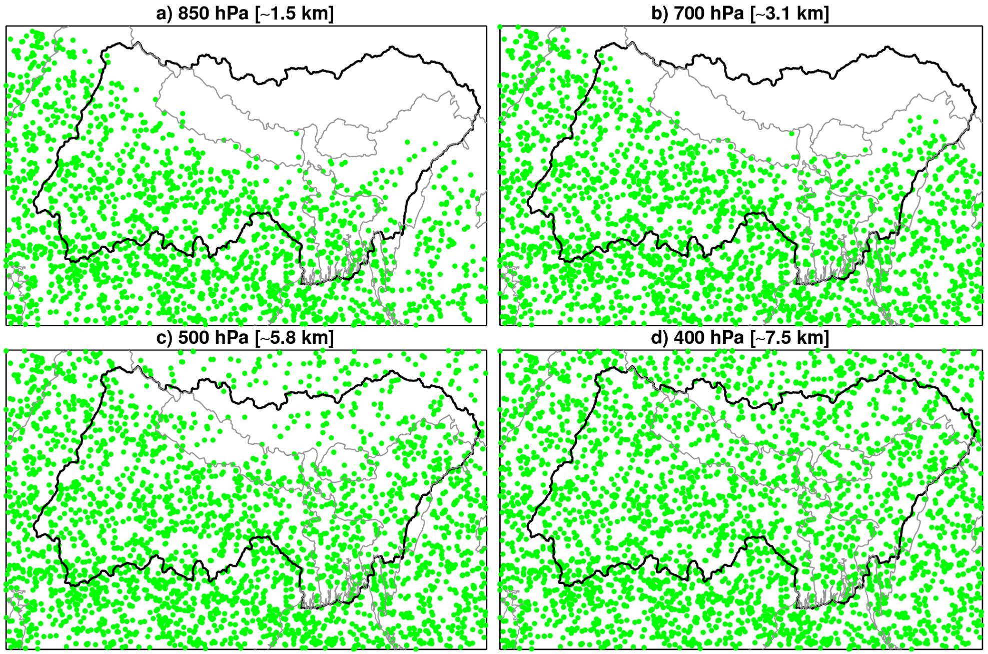

Figure 3. (a) Spatial distribution of COSMIC data points in the lower troposphere for the year 2012: **(a)** 850 hPa (∼ 1.5 km), **(b)** 700 hPa (∼ 3.1 km), **(c)** 500 hPa (∼ 5.8 km), and **(d)** 400 h Pa (∼ 7.5 km).

AMTD
8, 9399–9453, 2015

Interannual variability of UTLS over the GBM river basin

Khandu et al.

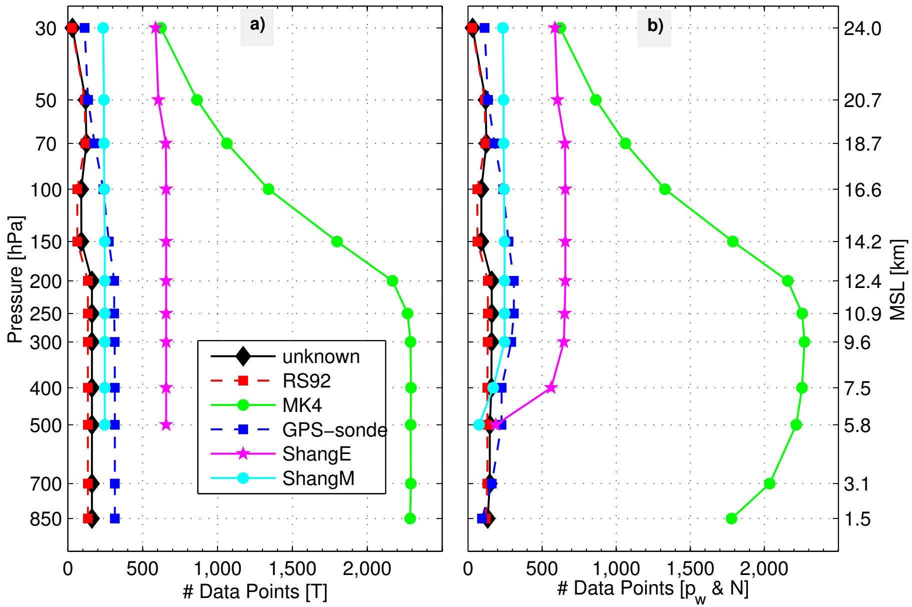

Figure 4. Number of data points at each pressure levels for temperature and humidity (water vapour pressure) of all the radiosonde types (see, Table 1) from August 2006 to December 2013.

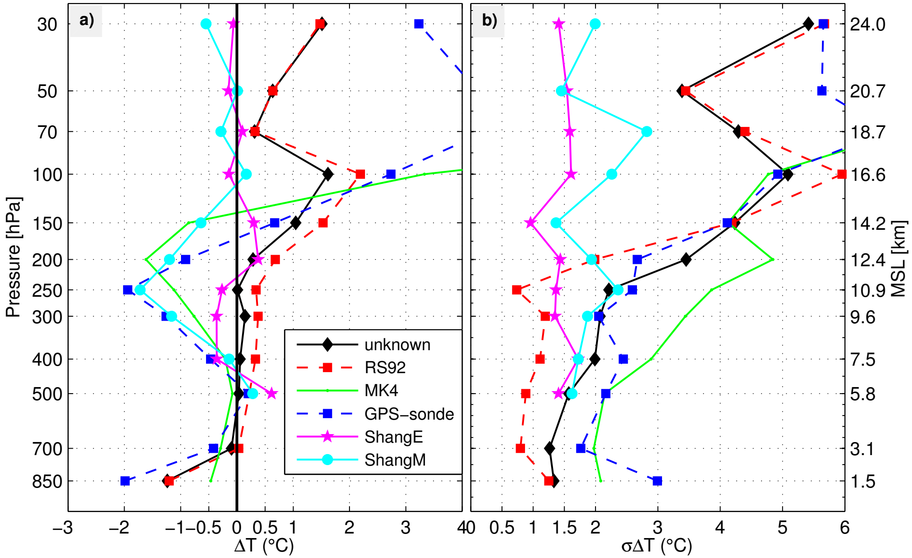

Figure 5. Mean temperature difference and standard deviations of various radiosonde types (refer to Table 1) with respect to COSMIC RO data over the GBM basin between August 2006 and December 2013.

AMTD
8, 9399–9453, 2015

Interannual variability of UTLS over the GBM river basin

Khandu et al.

Title Page
Abstract | Introduction
Conclusions | References
Tables | Figures
◀| |▶
◀ ▶
Back | Close
Full Screen / Esc
Printer-friendly Version
Interactive Discussion

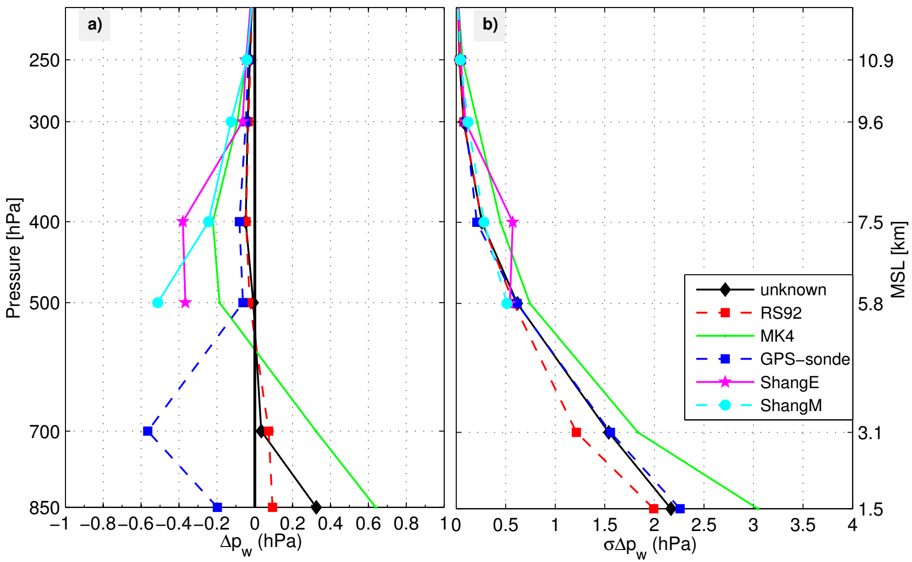

Figure 6. Mean differences and standard deviations of water vapour pressure (hPa) of various radiosonde types with respect to COSMIC RO data over the GBM basin between August 2006 and December 2013.

AMTD
8, 9399–9453, 2015

Interannual variability of UTLS over the GBM river basin

Khandu et al.

Title Page
Abstract | Introduction
Conclusions | References
Tables | Figures
◀| |▶
◀ ▶
Back | Close
Full Screen / Esc
Printer-friendly Version
Interactive Discussion

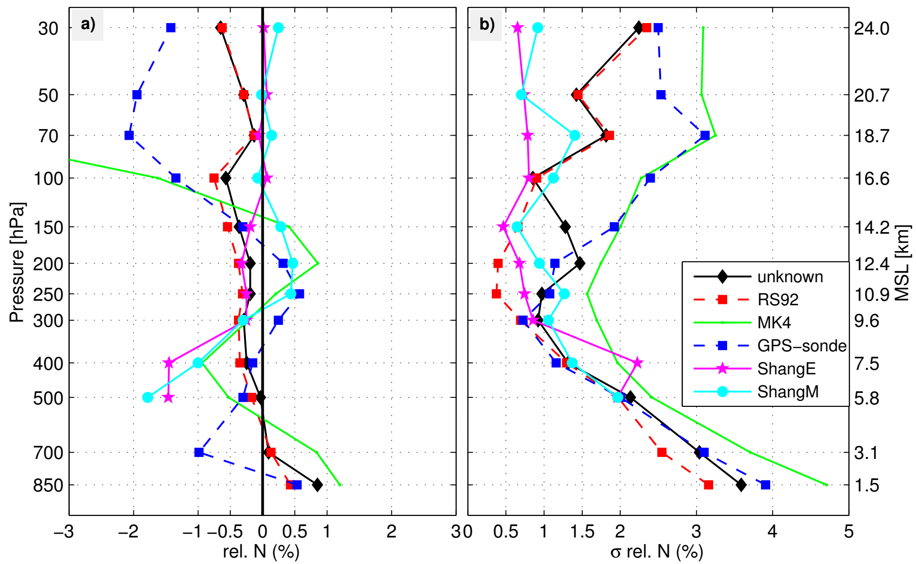

Figure 7. Relative mean differences and standard deviations of refractivity (in %) of various radiosonde types with respect to COSMIC RO data over the GBM basin between August 2006 and December 2013.

AMTD
8, 9399–9453, 2015

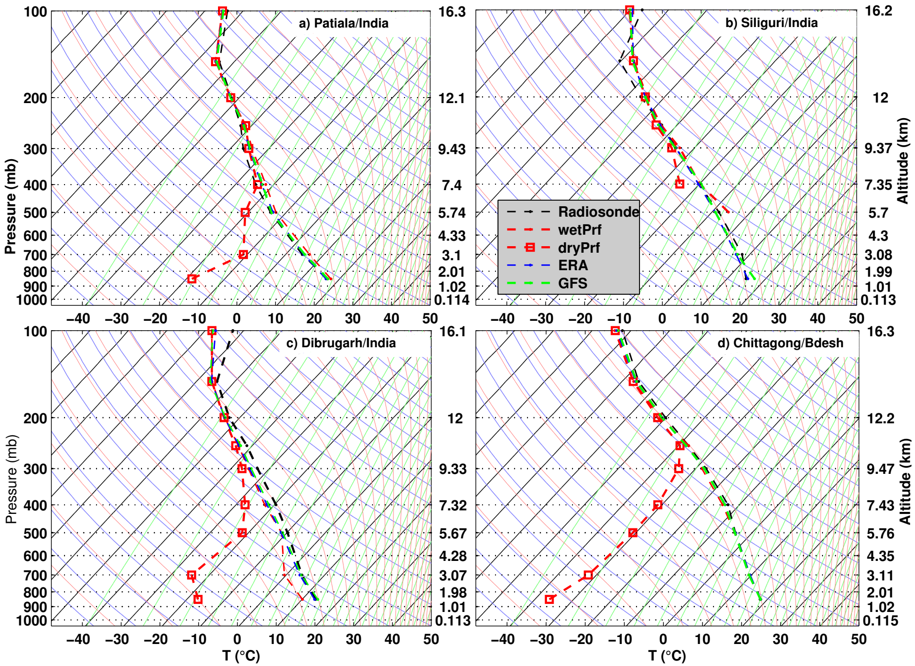

Figure 8. Comparison of mean air temperature from radiosonde, ERA-Interim, GFS and COSMIC profiles at **(a)** Patiala (India), **(b)** Siliguri (India), **(c)** Dirbugarh, and **(d)** Chittagong (Bangladesh) for 2012. Each station is an average of only 2 profiles. RS: radiosonde, ERA: ERA-Interim, GFS: Global Forecast Model, and wetPrf and dryPrf are the wet and dry profiles of COSMIC RO.

AMTD
8, 9399–9453, 2015

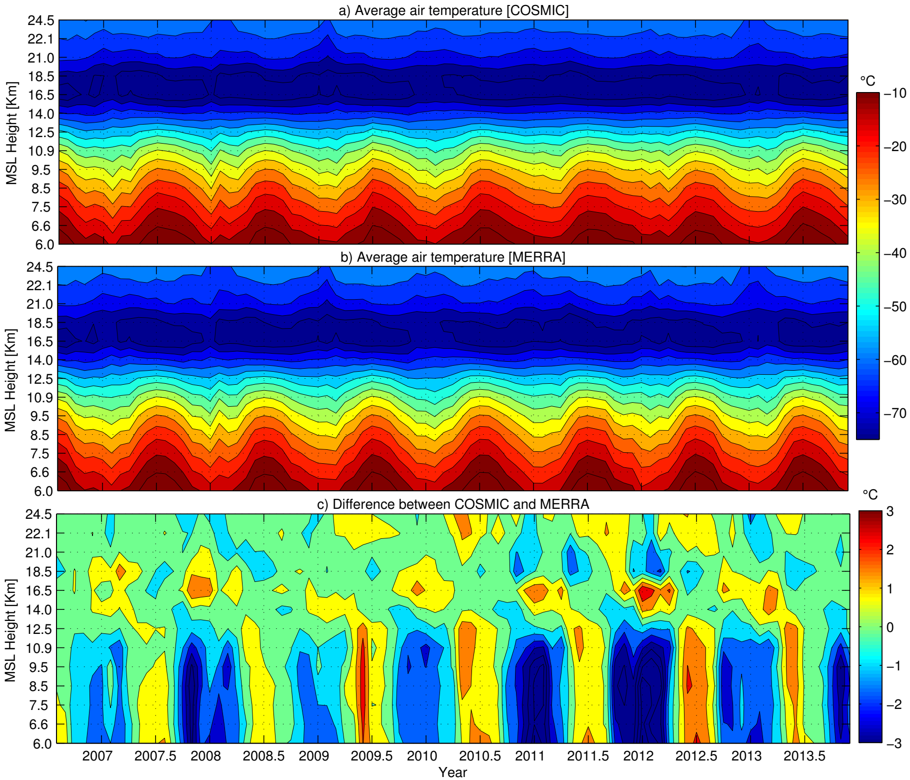

Figure 9. Mean air temperature between 500–30 hPa (or 6.0–24.5 km) for the period August 2006- December 2013. **(a)** COSMIC wet profiles, **(b)** MERRA re-analysis product, and **(c)** mean temperature difference between MERRA and COSMIC data.

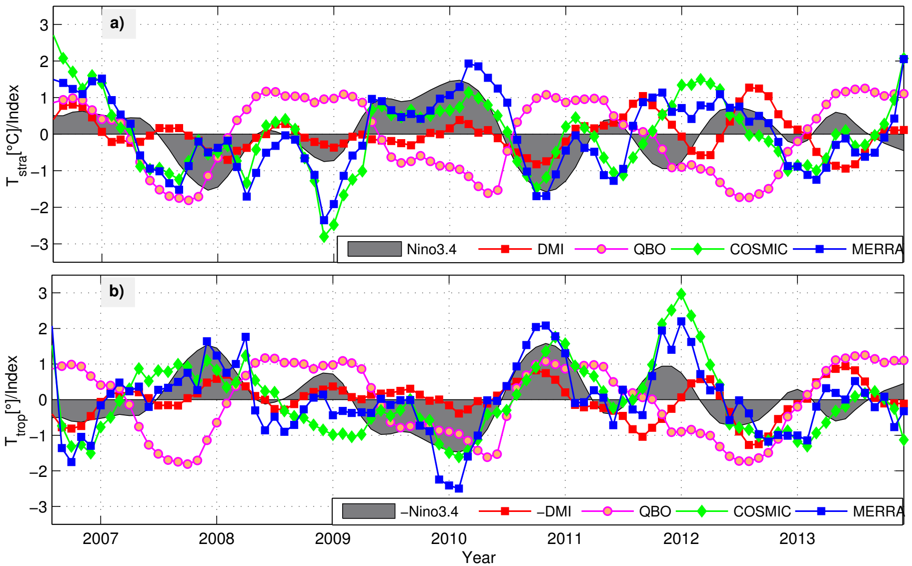

Figure 10. Interannual temperature variability of **(a)** LS (70–30 hPa; 18.5–24.5 km) and **(b)** UT (400–150 hPa; 7.5–14.0 km) based on MERRA data and COSMIC RO data from August 2006 to December 2013. QBO, ENSO and IOD indices are also shown. Note that **(b)** plots La Niña hence the opposite **(a)**.

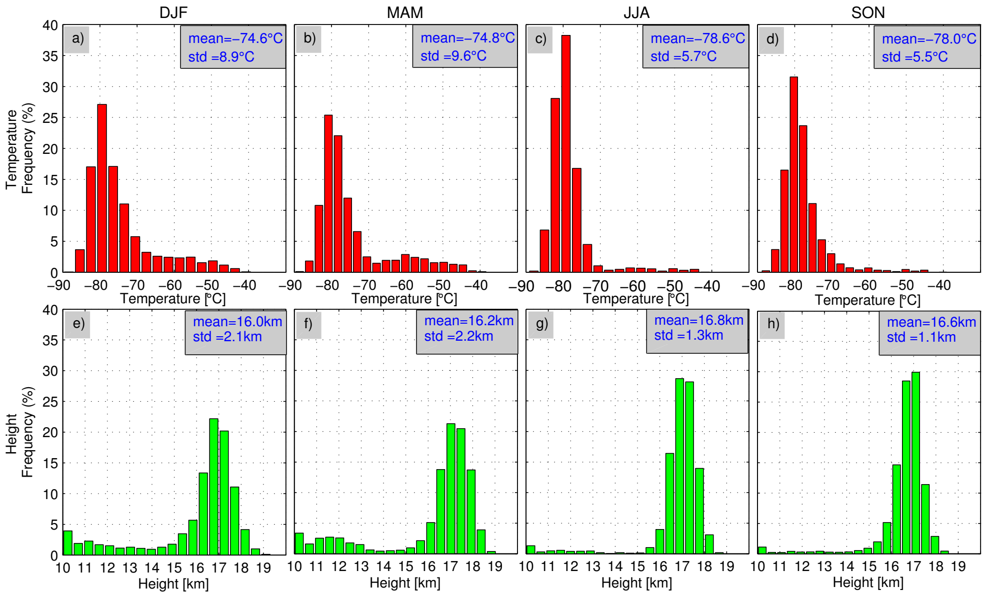

Figure 11. Frequency distribution of tropopause temperatures **(a–d)** and heights **(e–h)** over the GBM basin for the period between August 2006 and December 2013 based on COSMIC RO data.

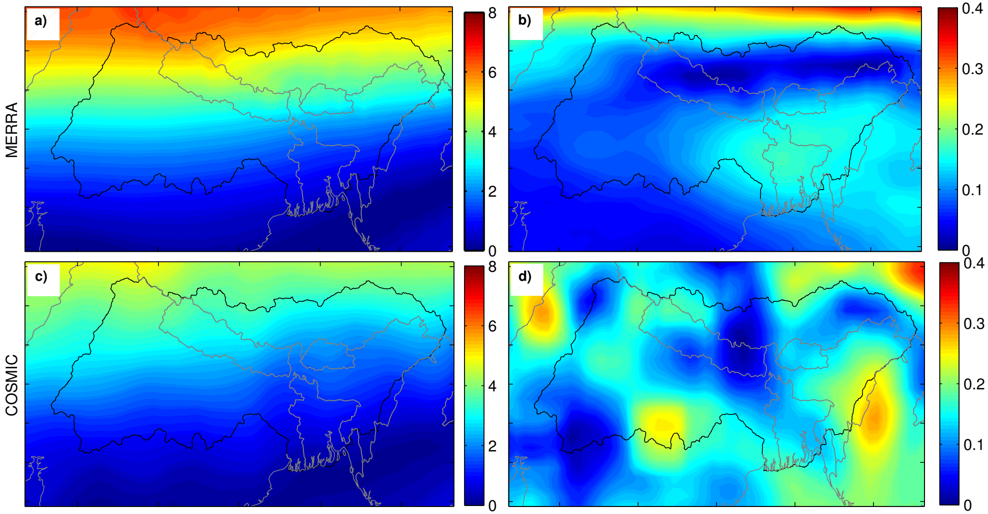

Figure 12. Annual and semi-annual amplitudes of tropopause temperatures (in °C) derived from MERRA (**a** and **b**) and COSMIC RO (**c** and **d**) data from August 2006 to December 2013. The annual amplitudes are scaled between 0–8 °C (**a** and **c**) and semi-annual amplitudes are scaled between 0–0.4 °C (**b** and **d**).

AMTD
8, 9399–9453, 2015

Interannual variability of UTLS over the GBM river basin

Khandu et al.

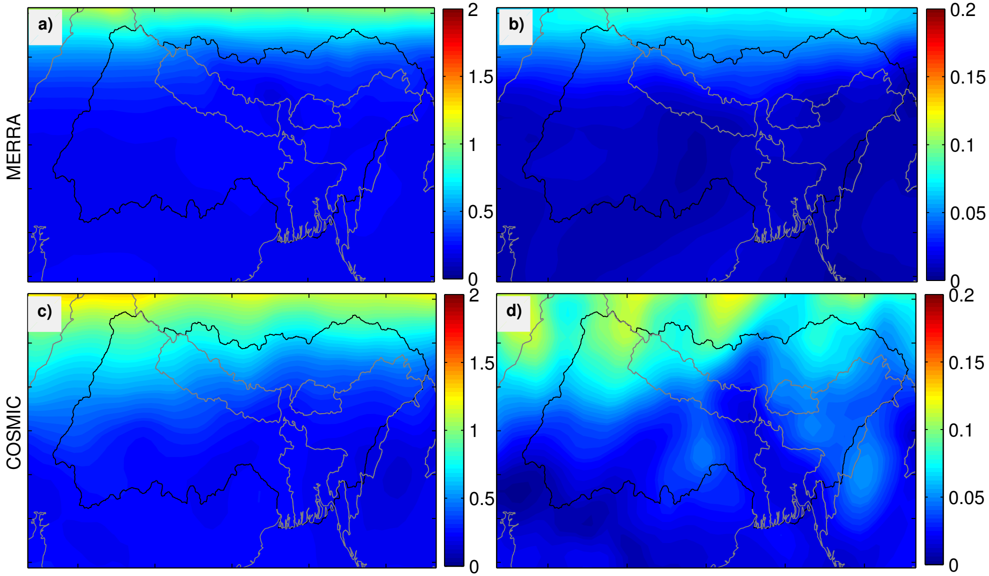

Figure 13. Annual and semi-annual amplitudes of tropopause heights (in km) derived from MERRA (**a** and **b**) and COSMIC RO (**c** and **d**) data from August 2006 to December 2013. The annual amplitudes are scaled between 0–2 km (**a** and **c**) and semi-annual amplitudes are scaled between 0–0.2 km (**b** and **d**).

AMTD
8, 9399–9453, 2015

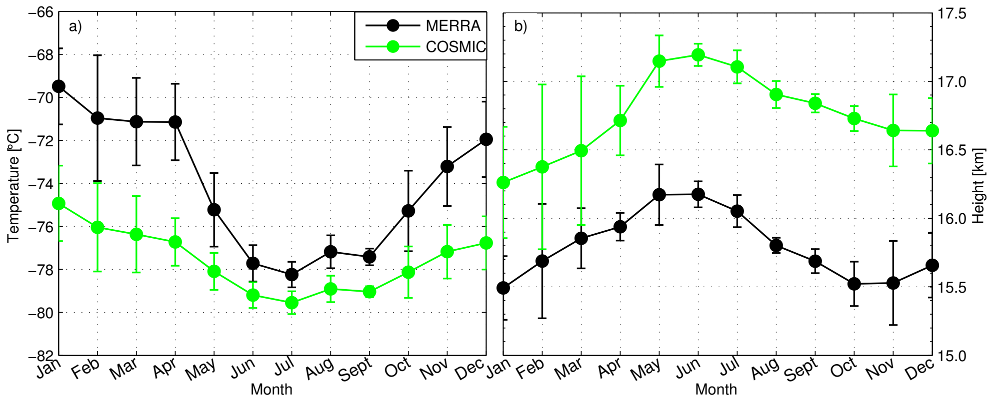

Figure 14. Annual cycle of tropopause over the GBM river basin computed from MERRA and COSMIC RO data for the period between August 2006 and December 2013: **(a)** tropopause temperatures, and **(b)** tropopause heights. The seasonal variations correspond reasonably well with Figs. 12 and 13 considering that factors impacting the interannual variabilities were effectivly removed in Figs. 12 and 13 based on the multi-linear regression approach in Eq. (4).

AMTD
8, 9399–9453, 2015

Interannual variability of UTLS over the GBM river basin

Khandu et al.

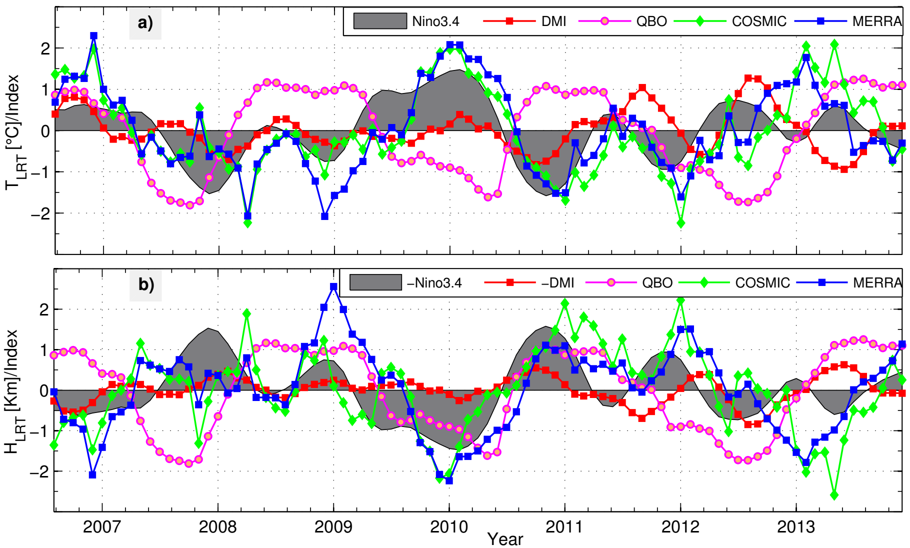

Figure 15. Interannual variability of tropopause temperatures and heights over GBM basin based on MERRA data and COSMIC RO data for the period August 2006 to December 2013, and their relations to major climatic indices in the region.

AMTD
8, 9399–9453, 2015

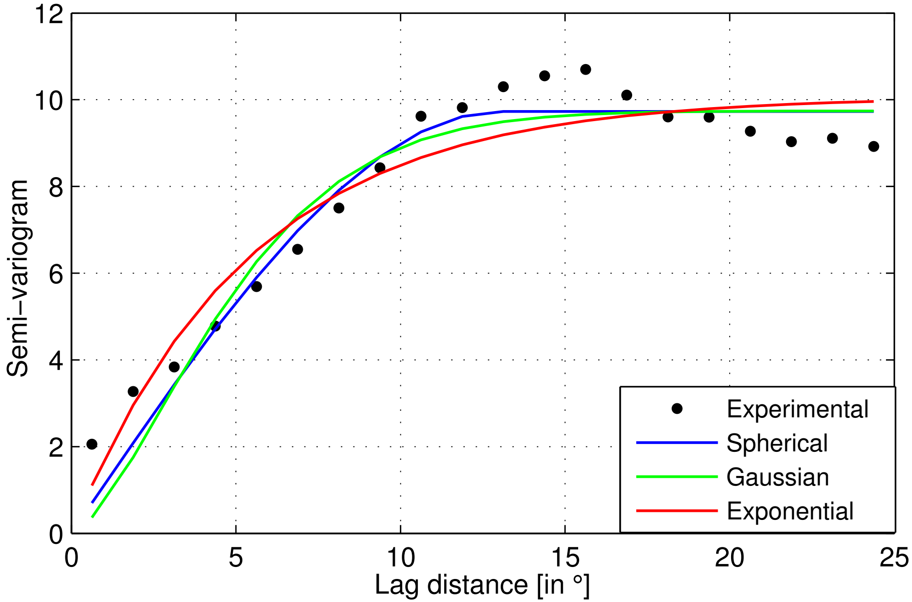

Figure 16. Semi-variogram of tropopause temperatures (September 2008) over the GBM basin based on COSMIC RO data.

AMTD
8, 9399–9453, 2015